Journal of Materials Chemistry A

REVIEW

View Article Online
View Journal | View Issue



Cite this: J. Mater. Chem. A, 2023, 11, 18502

# Recent advances in two-dimensional nanomaterials as bifunctional electrocatalysts for full water splitting

Cui Xu,[a] Mengyang Zhang,[a] Xianjun Yin,[a] Qiang Gao,[a] Shuai Jiang,[a] Junye Cheng,[d] Xin Kong,*[bc] Bin Liu *[a] and Hui-Qing Peng *[a]

Two-dimensional (2D) nanomaterials are some of the most promising bifunctional electrocatalysts that can simultaneously catalyze the hydrogen evolution reaction (HER) and oxygen evolution reaction (OER). They have attracted extensive attention owing to their decent electrocatalytic performance and cost advantages. In this review, we first provide an overview of 2D bifunctional electrocatalyst categories including layered double hydroxides, graphitic carbon nitride, metal–organic frameworks, transition metal dichalcogenides, and transition metal carbon/nitrogen compounds, and discuss their structures and synthesis methods, presenting detailed discussion on how the special 2D systems are synthesized and characterized experimentally, which complement a comprehensive understanding of the characteristics of 2D bifunctional electrocatalysts. Moreover, we focus on the recent development of 2D nano-catalysts with both HER and OER activity in the field of overall water splitting and summarize some typical strategies for enhancing the bifunctional activities, including doping, nanocomposite construction, interface formation, defect engineering and morphology modulation. The structure–activity relationships are also discussed with the aim of providing guidance in designing novel 2D bifunctional electrocatalysts. Finally, we explore some of the challenges and perspectives that remain in this rapidly growing field. We believe that the systematic and comprehensive contents of this review will stimulate wider research and attention.

Received 17th April 2023
Accepted 27th July 2023

DOI: 10.1039/d3ta02293e

rsc.li/materials-a



[a]State Key Laboratory of Chemical Resource Engineering, Beijing Advanced Innovation Center for Soft Matter Science and Engineering, College of Chemistry, Beijing University of Chemical Technology, Beijing, 100029, P. R. China. E-mail: binliu@buct.edu.cn; hqpeng@mail.buct.edu.cn

[b]Center of Super-Diamond and Advanced Films (COSDAF) and Department of Materials Science and Engineering, City University of Hong Kong, HK SAR, China

[c]Kunming University of Science and Technology, Department of Materials Science and Engineering, Kunming, 650504, P. R. China. E-mail: xinkong2-c@my.cityu.edu.hk

[d]Department of Materials Science, Shenzhen MSU-BIT University, Shenzhen, 517182, P. R. China

*Prof. Dr Hui-Qing Peng received her PhD from the Technical Institute of Physics and Chemistry, Chinese Academy of Sciences (CAS), under the supervision of Professor Chen-Ho Tung and Professor Qing-Zheng Yang in 2015. From 2015 to 2019, she was a postdoctoral fellow under the supervision of Prof. Ben Zhong Tang at the Hong Kong University of Science and Technology. After continued postdoctoral training with Prof. Wenjun Zhang at the City University of Hong Kong, she joined the Beijing University of Chemical Technology as a full professor. Her current research focuses on supramolecular photochemistry, aggregation-induced emission, two-dimensional nanomaterials, and catalysis.*

## 1. Introduction

With a growing population and rapid economic development, the global energy demand will continue to grow in the future. Fossil fuels (coal, oil, natural gas, *etc.*) have always been the main energy source for the global economy and society due to their high energy and easy access.[1] However, the overuse of fossil fuels has caused serious energy crises and environmental pollution. Therefore, it is significant to develop and utilize clean renewable energy to substitute conventional energies.[2] Hydrogen is a renewable, clean, zero-carbon-emission secondary energy. At present, most hydrogen is produced from fossil resources through steam reforming processes, which increases the consumption of fossil fuels and emissions of carbon dioxide. Among the developed technologies, producing molecular hydrogen from cheap and plentiful water through electrolysis technology has been widely regarded as a promising approach due to its simple conversion process, cleanliness, flexibility and high purity of hydrogen production.[3,4] Although water electrolysis technology has been developed and applied in the two centuries since it was first reported,[5,6] its widespread application is limited because of its high energy consumption and high cost.[7] The electrolytic water splitting reaction includes two half reactions: cathodic hydrogen evolution reaction (HER) and anodic oxygen evolution reaction (OER).[8] Depending on the reaction environment (acidic, neutral or basic), the two half-reactions of water electrolysis can be expressed in different ways as shown in Fig. 1.

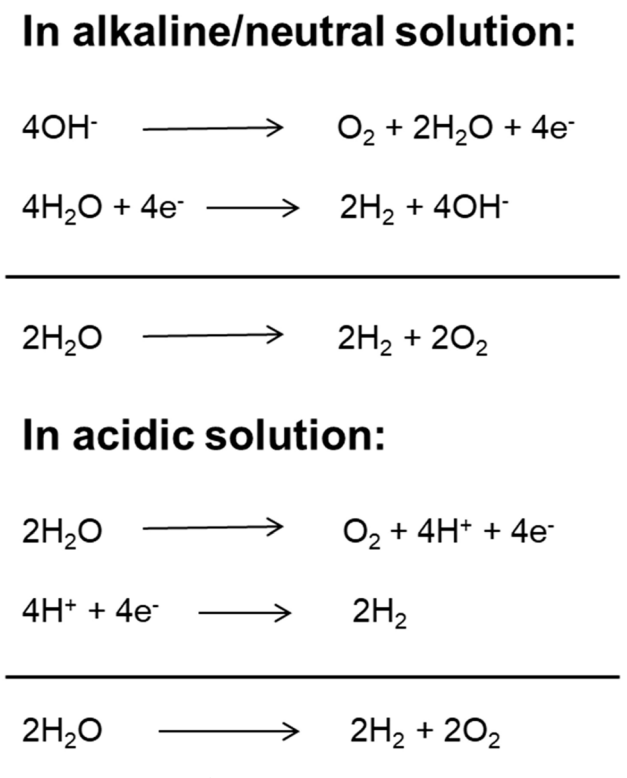


Fig. 1 The schematic of water splitting reactions under acidic, neutral and alkaline conditions.

Under standard conditions (25 °C and 1 atm), the $\Delta G$ of the water splitting reaction is 237.1 kJ $mol^{-1}$, corresponding to a thermodynamic potential of 1.23 V.[9] However, the adverse factors of electrode materials (such as activation energy and ion and gas diffusion) and device-related factors (such as solution concentration, wire and electrode resistance, electrolyte diffusion blockage, bubble formation, and heat release) result in a large overpotential during electrolysis. Therefore, the actual potential of water electrolysis is always far higher than the theoretical minimum value (commercial cells usually work at a voltage of 1.8–2.0 V).[10] Therefore, exploring suitable catalysts to reduce the reaction overpotential and increase the reaction rate and thus the total electrolysis efficiency is the current research direction. An ideal catalyst for water electrolysis must meet two basic requirements. First, the catalyst must be highly active and have a minimum overpotential to produce a high current density. Second, the catalyst must have long-term stability. Hence, the development of electrocatalysts possessing high activity and stability will be favorable for the advancement of the large-scale applications of electrolysis-related technologies. Earlier, Pt was used for the HER, while $RuO_2$ and $IrO_2$ were used for the OER.[11–15] However, their scarcity, high cost and non-bifunctional properties hamper the application in large-scale water splitting. In most of the cases, the electrocatalysts show high HER performance but worse performance for the OER in acidic medium, and high OER performance but inferior performance for the HER in alkaline medium.[16] At the same time, to meet the practical application requirements, the HER and OER should be carried out in the same electrolyte utilizing a single catalyst to achieve full water splitting. However, the current prevailing water splitting requires the integration of two types of catalysts that are especially suitable for the HER and OER, respectively. Such a combination is usually incompatible and thus results in a poor overall performance. Therefore, the development of bifunctional catalysts, which are highly active for both the HER and OER, is of prime importance for full water splitting.

Two-dimensional (2D) nanomaterials are regarded as some of the most promising electrocatalysts for the HER and OER.[17–22] The significance and irreplaceability of 2D nano-catalysts can be demonstrated as follows: (1) 2D nanomaterials have high specific surface areas (maximal surface to bulk ratio), copious surface and edge-exposed sites, high morphological anisotropy, tunable chemical composition, and unique electronic structure; (2) most 2D catalysts could serve as ideal platforms to couple with other materials or substrates compared with the bulk catalyst; (3) 2D catalysts can be easily activated and optimized for enhanced activity by some activation strategies; (4) 2D catalysts can be used as an ideal model to investigate the relationship between the exposed active sites and the catalytic activity, revealing the catalytic mechanism. In 2004, Geim and Novoselov isolated graphene for the first time by stripping graphite.[23] Since then, researchers have discovered a series of 2D nanomaterials with similar layered structural characteristics, including layered double hydroxides (LDHs), graphite phase carbon nitride (g-$C_3N_4$), 2D metal–organic frameworks (MOFs), transition metal dichalcogenides (TMDs) and

transition metal carbon/nitrogen compounds (MXenes) and 2D metal nanomaterials, which have attracted extensive research interest in electrocatalytic due to their unique surface chemistry properties and high specific surface area. With the development of electrocatalysts used for water electrolysis, 2D nanomaterials have been found to be electrocatalytically active toward the OER or HER. In particular, 2D bifunctional catalysts that can simultaneously catalyze the HER and OER (*i.e.*, full water splitting) have attracted extensive attention because of their decent catalytic performance and cost advantage. In spite of the great advances, no review is available that is exclusively dedicated to introducing the advances in 2D nanomaterials as bifunctional electrocatalysts for full water splitting, with a particular emphasis on activation strategies for improving bifunctional catalytic activities so far. Moreover, the catalytic activity origin of electrocatalysts is unclear due to the frequent lack of deep insights into the catalytic reaction mechanism at the atomic level, and especially the discussion of the effect of their electronic structure and morphology on catalytical properties is still limited.[24–26] Thus, we would like to make a comprehensive summary and induction of the progress of 2D electrocatalysts used for overall water splitting (considering the relatively limited reports on 2D metal nanomaterials as bifunctional electrocatalysts,[27–29] this review does not introduce it detail), so as to provide reference and guidance for researchers in related fields.

In this review, we will first provide an overview of 2D bifunctional electrocatalyst categories, including layered double hydroxides, graphitic carbon nitride, metal–organic frameworks, transition metal dichalcogenides, and transition metal carbon/nitrogen compounds, and discuss their structures and synthesis methods, presenting detailed discussion on how the special 2D systems are synthesized and characterized experimentally which will complement a comprehensive understanding on the characteristics of 2D bifunctional electrocatalysts. Then, we will summarize the effective activation strategies of 2D bifunctional electrocatalysts including doping, defect engineering, nanocomposite construction, interface formation and morphology engineering (Fig. 2). Meanwhile, the relationship between the structure and performance of 2D catalysts will be discussed. Finally, perspectives on the challenges and opportunities in developing new 2D cost-effective and high-efficiency bifunctional electrocatalysts for practical applications will be outlined, which will provide valuable insights for the development of novel 2D bifunctional electrocatalysts with high performance.

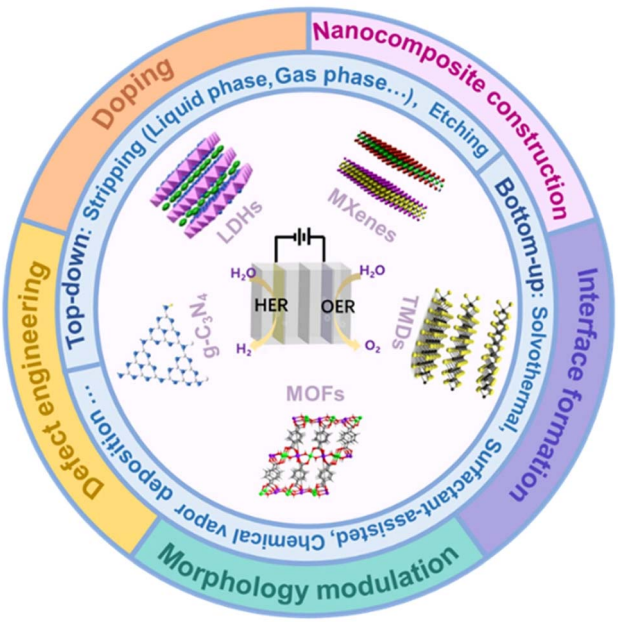


Fig. 2 The schematic picture showing two-dimensional nanomaterials about their structures, synthesis methods and activation strategies in the field of overall water splitting.

## 2. Structure of two-dimensional nanomaterials

### 2.1 Layered double hydroxides (LDHs)

LDHs are a class of 2D anionic clay materials, which is a general term for hydrotalcite and hydrotalcite like compounds. As shown in Fig. 3a, their general expression is $[M^{2+}_{1-x}M_x^{3+}(OH)_2]^{x+}[A_{x/n}{}^{n-}]\cdot mH_2O$,[1] where $M^{2+}$ and $M^{3+}$ represent the metal cations respectively, and $m$ represents interlamellar water volume. $A_{x/n}{}^{n-}$ is the intercalation anion, and the $x$ value is equal to the mole ratio of $M^{2+}/(M^{2+}+M^{3+})$, and the $x$ value ranges from 0.2 to 0.33. In terms of expression, LDHs are mainly composed of three parts: main laminate, interlayer anions and solvent molecules. The main laminate is composed of divalent metal cations $M^{2+}$ ($Ca^{2+}$, $Fe^{2+}$, $Mg^{2+}$, $Zn^{2+}$, *etc.*) and trivalent metal cations $M^{3+}$ ($Fe^{3+}$, $Ni^{3+}$, $Ti^{3+}$, $Cr^{3+}$, *etc.*). The interlayer is mainly occupied by intercalated anions ($OH^-$, $NO_3{}^-$, $CO_3{}^{2-}$, $HCO_3{}^-$, *etc.*), and solvent molecules are mainly water molecules between the main laminates.[30] Generally speaking, $M^{2+}$ and $M^{3+}$ metal ions are the active sites in catalytic reactions of LDHs.[31,32] LDHs with different properties and functions can be obtained by adjusting the type of metal cation, the mole ratio of $M^{2+}/M^{3+}$ and the anions in solution. LDHs have attracted great interest in energy storage/conversion, chemical sensing, magnetism, optics, biomedical science, and other fields due to their tunability of composition and the structure, simplicity of the synthesis process and uniqueness of physical and chemical properties.[33–39] At present, many kinds of LDHs are successfully applied in the catalytic electrolysis of water reaction and show good results due to their excellent electrical conductivity and structural stability. Since 2009, there has been an explosion of publications on LDH-based materials employed as efficient electrocatalysts.[39–41] In order to promote the performance of LDH-based electrocatalysts, some strategies including modification of carbon materials, defect engineering, and loading of noble metals could be adopted, which will be discussed in a later chapter.

### 2.2 Graphite phase carbon nitride (g-$C_3N_4$)

g-$C_3N_4$, a metal-free polymeric material, is one of the oldest 2D materials in the record of scientific literature, and has a high nitrogen content and similar planar structure to graphene.[42] Its

 

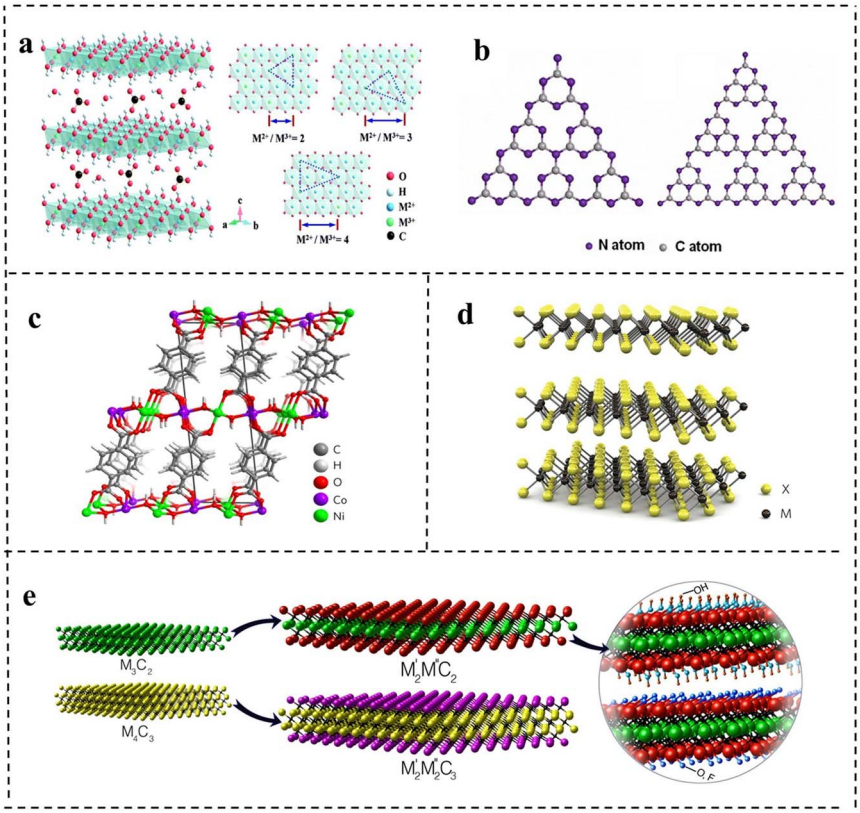


Fig. 3 The schematic structures of (a) layered double hydroxides (LDHs). Reproduced with permission from ref. 30. Copyright 2020, Elsevier. (b) Graphite phase carbon nitride (g-$C_3N_4$). Reproduced with permission from ref. 46. Copyright 2017, American Chemical Society. (c) Metal–organic frameworks (MOFs). Reproduced with permission from ref. 56. Copyright 2016, Springer Nature. (d) Transition metal dichalcogenides (TMDs). Reproduced with permission from ref. 61. Copyright 2012, Springer Nature. (e) Transition metal carbon/nitrogen compounds (MXenes). Reproduced with permission from ref. 66. Copyright 2015, American Chemical Society.

history can be traced back to 1834, when Berzelius successfully synthesized a carbon nitride compound, which was named by Liebig. Subsequently, in 1996, Teter *et al.*[43] used first-principles methods to accurately calculate the structure of carbon nitride compounds and proposed five different crystal structures of carbon nitride: α-$C_3N_4$ phase, β-$C_3N_4$ phase, cubic $C_3N_4$ phase, quasi-cubic $C_3N_4$ phase and graphite-like $C_3N_4$ phase. Among them, the structure of graphite-like $C_3N_4$ (g-$C_3N_4$) is the most stable. The highly delocalized π conjugated system is formed by $sp^2$ hybridization between C atoms and N atoms. Studies have found that the basic structural units of g-$C_3N_4$ are two allotropes of g-$C_3N_4$, a triazine ring ($C_3N_3$) and a heptazine ring ($C_6N_7$) (as shown in Fig. 3b).[44–46] Kroke *et al.*[47] calculated the binding energy of the heptazine ring unit by first-principles density functional theory (DFT), and it was 30 KJ $mol^{-1}$, much lower than that of the triazine ring, indicating that g-$C_3N_4$ composed of the heptazine ring was more stable than the triazine ring. Therefore, the heptazine ring is generally considered to be the typical structure of g-$C_3N_4$. g-$C_3N_4$ with a heptazine ring as the structural unit is formed by $sp^2$ hybridization, so a π conjugated plane is formed between rings through the connection of N atoms at the end of the rings, which shows considerable chemical stability (stable in acids, alkalis, and various organic solvents), thermal stability (up to 600 °C in air) and an appealing electronic structure with a suitable bandgap.[48] At the same time, layers are connected by weak van der Waals force. Thus, g-$C_3N_4$ has a broad application prospect in the field of catalysis, triggering a lot of research work.

At present, g-$C_3N_4$ is widely used in catalytic reactions due to its advantages of highly active sites, easy preparation, low cost and excellent photoelectric chemical properties. The application of g-$C_3N_4$ in electrochemical catalysis was first studied in 2009. Lyth *et al.*[49] first demonstrated that g-$C_3N_4$ had higher oxygen reduction catalytic activity than carbon black in an acidic environment, but its ultralow specific surface area and weak electrical conductivity limited its catalytic activity. After mixing g-$C_3N_4$ with carbon black, the specific surface area and conductivity of the catalyst were improved and the activity was obviously enhanced. Pure g-$C_3N_4$ based compounds are not competitive in the field of electrocatalysis and have low current densities even at very high overpotentials because of the weak electrical conductivity. However, the activity of g-$C_3N_4$ can be optimized by means of hybridizing with carbon-based materials, metal or non-metal doping, and regulating the morphology and nanostructure. Since then, some researchers began to study modified g-$C_3N_4$ materials in depth to achieve enhanced catalytic activity, which had been successfully applied in water electrolysis to catalyze the HER and OER.

### 2.3 Metal–organic frameworks (MOFs)

A metal–organic framework is a kind of organic–inorganic hybrid material with intramolecular pores formed by self-assembly of metal ions or clusters and organic ligands through coordination bonds.[50] In layered MOFs, there are strong in-plane coordination bonds, but weak interactions between layers (*e.g.*, van der Waals forces and hydrogen bonding) as shown in Fig. 3c.[42] In 1995, Yaghi *et al.*[51] successfully synthesized 2D structural MOF materials by reacting the transition metal Co with 1,3,5-benzenetricarboxylic acid and proposed the concept of metal–organic frameworks for the first time. Different from inorganic porous materials and general organic complexes, MOFs have both the rigidity of inorganic materials and the flexibility of organic materials, possessing a designable structure, large channel, and high surface area. Basically, the metal nodes can serve as active sites for the catalytic process. Therefore, so far, MOFs have been reported to be widely used in gas storage, biocatalysis, photocatalysis, chemical sensing and other fields.[52] However, when MOFs are used in electrocatalysis, the main problems are poor electrical conductivity and the instability of their own structure caused by metal nodes surrounded by organic linkers compared with other 2D nanomaterials.[53,54] Accordingly, researchers have made some progress in increasing the electrical conductivity and stability of MOFs for good electrocatalytic performance by combining different metal ions or metal clusters with different organic ligands to adjust the structure.[55] Many studies have shown that 2D MOFs have unique characteristics compared with gross phase MOFs, which have great potential in the field of electrocatalysis.[56–58] 2D MOFs allow more active sites to be exposed on the surface. Due to the lack of organic ligands, the metal sites on the surface are unsaturated, which greatly improves the catalytic activity.[59] In addition, the ultrathin structure can provide a short diffusion path and fast electron charge transfer, further enhancing the catalytic activity. The diverse and tunable chemical structures of 2D MOFs provide a convenient way to fabricate a variety of efficient catalysts with bifunctional catalytic activity by expanding the surface area, incorporating bimetallic components and combining non-metallic elements. 2D MOFs also introduce better simplicity and compatibility for electrocatalytic systems. Despite many advantages, the research on bifunctional MOF-based catalysts is still in the initial stage, which faces several challenges in academic research and industrial applications.

### 2.4 Transition metal dichalcogenides (TMDs)

Transition metal dichalcogenides are another class of 2D materials that have been extensively investigated following the unconventional properties of graphene. TMDs have attracted extensive attention because of their broad energy application prospects and striking fundamental properties.[60] TMDs can be described by the chemical formula of $MX_2$, where M refers to transition metal elements such as molybdenum (Mo), tungsten (W), niobium (Nb) and rhenium (Re). It is sandwiched between two chalcogenide $X_2$ such as sulfur (S), selenium (Se) and tellurium (Te) with a thickness of $\leq$1 nm. The atoms are covalently bonded within each layer (X–M–X), and the individual layers are connected together through weak van der Waals (vdW) forces with +4 state metal and −2 state chalcogen atoms. Due to the presence of lone pairs of chalcogen atoms terminating the surface of the layers and the resulting difference in oxidation states, a significant amount of ionic character is induced between the metal and chalcogen atoms. $MX_2$ layered structures have three thermodynamically stable structures: 2H (hexagonal symmetry and triangular prism coordination, with two layers in each repeating unit), 3R (rhombic symmetry and triangular prism coordination, with three layers in each repeating unit) and 1T (tetragonal symmetry and octahedral coordination, with one layer in each repeating unit) with a spacing of 0.7 nm (as shown in Fig. 3d).[61] The unique structure of TMDs can also be visualized from the perspective of two distinct orientations characterized by surface inertness (basal planes) and high surface energy (edges), exhibiting anisotropic properties. It has been revealed that the electrical conductivity along the layer is $\approx$2200 times higher than that across the van der Waals force gaps between layers, predicting much faster electron transport at the edges compared to the basal planes.[62] Such inherent characteristics of TMDs can give rise to prominently active catalysis in electrocatalytic reactions provided that the active edges are maximally exposed.[63,64]

### 2.5 Transition metal carbon/nitrogen compounds (MXenes)

MXene is a new kind of 2D material, which is divided into transition metal carbide and nitride. In 2011, Gogotsi *et al.*[65] for the first time obtained a 2D layered transition metal carbon/nitride material (named MX) after selective etching of the A atom layer in a MAX phase. MAX phases are a large family of layered ternary transition-metal carbides or nitrides with the chemical formula $M_{n+1}AX_n$ ($n$ = 1, 2, or 3), where M is a transition metal, A is an A-group element (usually IIIA or IVA group), and X is C or N. Since the M–A bond is weaker than the M–X bond, the "A" atomic layer can be selectively etched from the maximum phase using HF. Compared with the crystal structure of MAX phases, the A atomic layer of MX is missing, and the 2D structure is similar to that of graphene, so it is named MXene. There has been an exponential increase in the number of reports on MXene materials thus far. Researchers have traditionally defined the general formula for the MXene structure as $M_{n+1}X_nT_x$, where $n$ = 1–3, $T_x$ represents surface termination groups, such as –OH, –O, or –F (the structures are shown in Fig. 3e)[66] and studies showed that the stoichiometric coefficient ratios of MXenes are $M_2X$, $M_3X_2$ and $M_4X_3$ respectively.[67,68] MXene materials have a layered structure with van der Waals force and hydrogen bonding between the adjacent layers, a highly adjustable transition metal combination structure and a large specific surface area. In addition, MXenes also exhibit excellent charge transfer kinetics meaning good electrical conductivity compared with other 2D nanomaterials, and the –OH functional group on the surface can interact with polar solvents such as water and ethanol, showing good hydrophilicity.[69–71] All of these properties make MXenes an effective electrocatalyst. As a class of young 2D nanomaterials,

 

MXenes feature high electrical conductivity, hydrophilicity, and adjustable surface properties, and exhibit great potential in overall water splitting as electrocatalysts. In 2016, $Mo_2CT_x$ and $Ti_3C_2Tx$ were reported for the first time as HER and OER catalysts, respectively. Since then, the number of MXene papers in the field of water splitting has increased year by year.[72,73]

# 3. Synthesis method

## 3.1 Top-down

At present, the methods of synthesizing 2D materials are mainly divided into top-down and bottom-up methods. Top-down synthesis is usually the decomposition process of layered or massive materials under the action of external forces. The key to this approach is to destroy the van der Waals forces, hydrogen bonds or π–π stacking between the layered structures, and further delaminate the layered structures to 2D ultrathin nanosheets. There are many top-down synthesis methods for 2D nanomaterials, including liquid phase stripping, gas phase stripping, ultrasonic stripping, mechanical stripping, intercalation/chemical stripping, etching, *etc.*

**3.1.1 Liquid phase stripping.** Liquid phase stripping is one of the most commonly used methods to prepare 2D nanomaterials. By introducing guest molecules, the interaction between layers can be reduced. In 2005, Sasaki *et al.*[74] mixed $Mg_2Al$-LDH with formamide and successfully separated a large-size LDH for the first time. Delaminated nanosheets had a lateral size of several micrometers and a thickness of 0.8 nm, as verified by atomic force microscopy (AFM) observation (Fig. 4a). Formamide is a kind of good interlaminar growth inhibitor, that can reduce interlaminar interaction and prevent lamellar stacking. Later, Hu *et al.*[75] also successfully prepared NiFe, NiCo and CoCo-LDH nanosheets in formamide (Fig. 4b). Pumera *et al.*[76] used the liquid stripping strategy to strip bulk $MoS_2$ by using different organic lithium compounds (*n*-BuLi, Me–Li and *t*-BuLi) as shown in Fig. 4c. It is revealed that the stripping process of bulk $MoS_2$ was related to the molecular size of the organic lithium compound. Following the sequence of molecular size (Me–Li < *n*-Bu–Li < *t*-Bu–Li), the stripping process was more and more effective. $MoS_2$ produced by *n*-Bu–Li and *t*-Bu–Li stripping was more active for the HER than $MoS_2$ produced by Me–Li stripping (Fig. 4d and e). Zhang *et al.*[77] separated ultra-thin g-$C_3N_4$ nanosheets in water by the liquid phase stripping method (diameter of ~70–160 nm and thickness of ~2.5 nm). The nanosheets could be stably suspended in acidic and alkaline media for one week, and the density of states of single-layer g-$C_3N_4$ nanosheets in the conduction band increased significantly compared with that of the bulk counterpart. Yang *et al.*[78] also peeled off g-$C_3N_4$ nanosheets with a thickness of ~2 nm using isopropanol as the medium by using the liquid phase stripping method. In 2015, Lin *et al.*[79] used different proportions of mixed solvents, including ethanol and water, isopropylamine and water, and *N*,*N*-dimethylformamide (DMF) and water, to peel the bulk phase of g-$C_3N_4$. It was found that the use of mixed solvent was more conducive to the preparation of high concentration g-$C_3N_4$ nanosheet suspension. Compared with the bulk, the prepared anisotropic

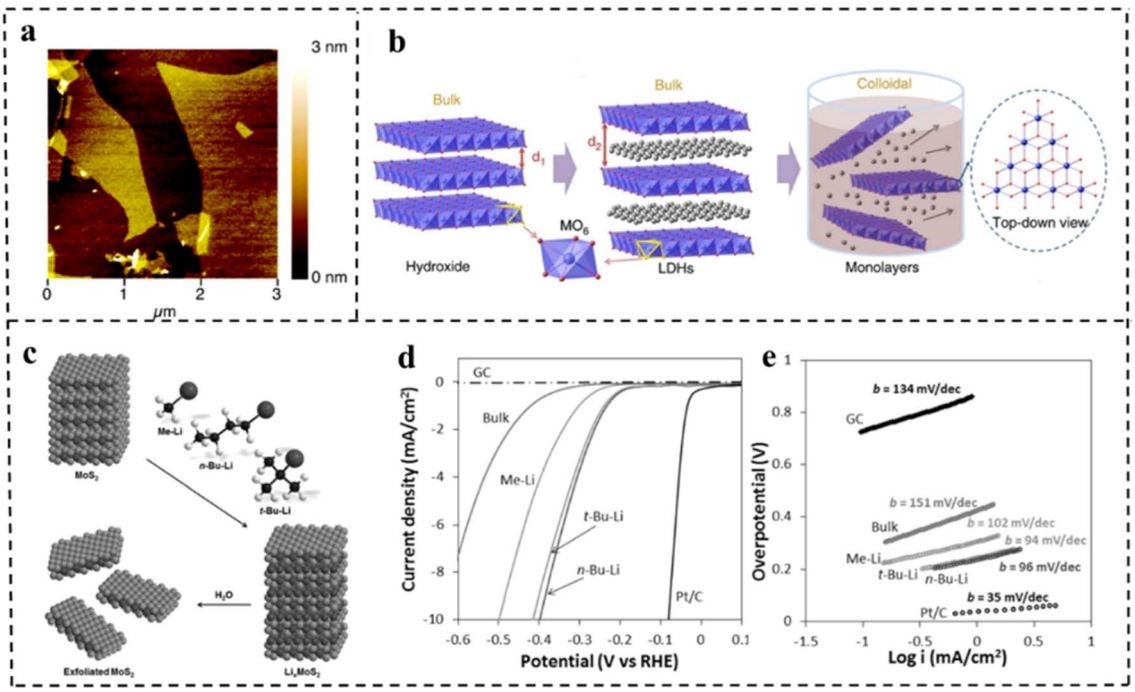


Fig. 4 (a) AFM image of delaminated MgAl-LDH sheets. Reproduced with permission from ref. 74. Copyright 2005, American Chemical Society. (b) Schematic representation of LDH nanosheets' synthesis and structures. Reproduced with permission from ref. 75. Copyright 2014, Springer Nature. (c) Schematic representation of exfoliation of $MoS_2$ with methyllithium, *n*-butyllithium and tert-butyllithium. (d) Polarization curves and (e) corresponding Tafel plots for $MoS_2$ with different exfoliation media and other control materials. Reproduced with permission from ref. 76. Copyright 2015, Wiley-VCH.

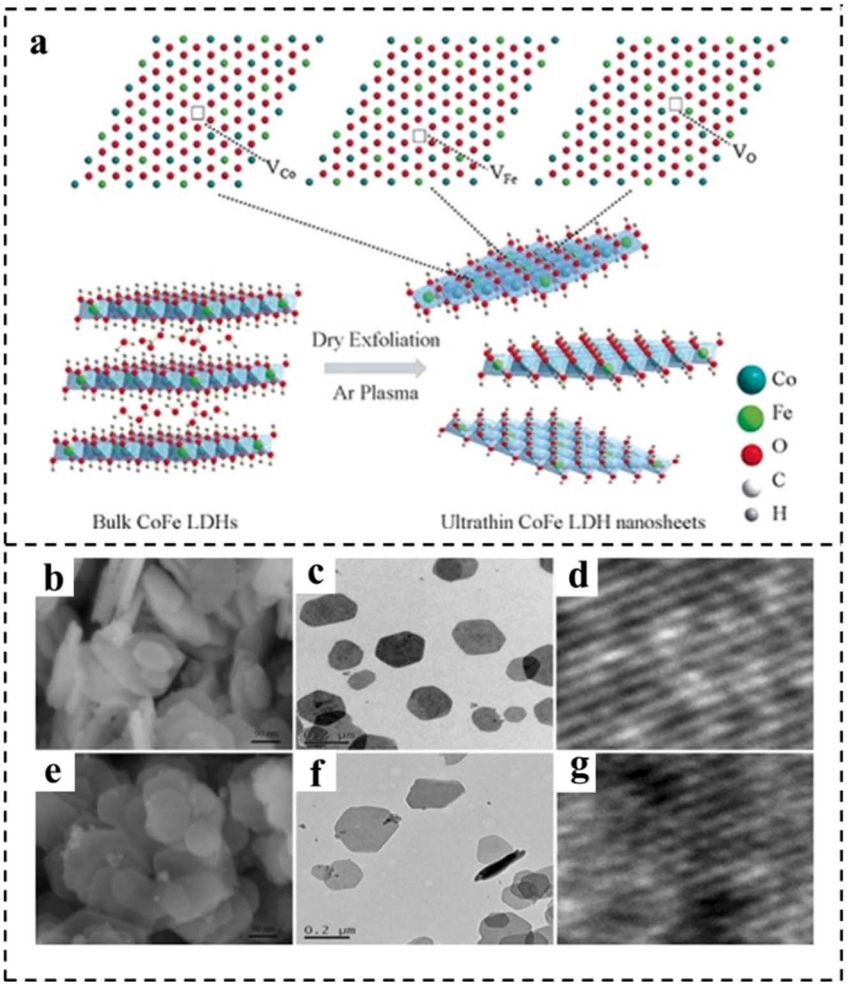


Fig. 5 (a) Schematic representation of CoFe LDH nanosheets obtained by Ar plasma exfoliation. Scanning electron microscope (SEM), transmission electron microscope (TEM), and high resolution transmission electron microscope (HRTEM) images of (b–d) the bulk CoFe LDHs and (e–g) the ultrathin CoFe LDHs–Ar nanosheets. Reproduced with permission from ref. 80. Copyright 2017, Wiley-VCH.

2D nanosheets had a larger specific surface area and more active sites, which exhibited better OER activity.

**3.1.2 Gas phase stripping.** The nanosheets obtained by liquid phase stripping have strong adsorption to solvent molecules, which hinders the exposure of surface active sites and thus reduces catalytic activity. Moreover, once the solvent molecules are removed, the nanosheets formed by stripping may stack again. In this regard, gas phase stripping can overcome this problem. Wang *et al.*[80] for the first time used Ar plasma to strip large CoFe LDHs into ultrathin LDH nanosheets (thickness of ~0.6 nm) (as shown in Fig. 5e–g). Various vacancies (including oxygen, cobalt and iron vacancies) were formed in the stripping process, which is conducive to regulating the electronic structure of the material and reducing the coordination numbers around cobalt and iron atoms (Fig. 5a). This is beneficial to the adsorption/desorption behavior optimization of OER intermediates on the LDH surface. Besides, the ultrathin structure of 2D LDH nanosheets compared with bulk CoFe LDHs (Fig. 5b–d) also exposes more active sites and significantly improves the OER activity. Furthermore, Ar plasma stripping is not only clean, efficient and non-toxic, but also can obtain stable nanosheets in a powder state.

**3.1.3 Ultrasonic stripping.** Ultrasonic stripping is one of the simplest methods to obtain high quality 2D nanomaterials. In the ultrasonic stripping process, the original bulk material in a specific solvent is exposed to ultrasonic waves, resulting in the acoustic cavity effect. The continuous nucleation, growth and collapse of bubbles provide enough energy to break the interplanar forces within the 2D material to achieve stripping. In 2008, Nielsen *et al.*[81] first used ultrasonic vibration to peel metal–organic compounds. The weak interlayer interaction can be easily overcome by ultrasonic stripping to peel MOFs into 2D nanosheets. Then, a series of MOFs were successfully stripped into nanosheets, including $[Cu_2Br(IN)_2]$ N (IN = isonicotinic acid) nanosheets[82] and $Zn_2(BIM)_4$ (BIM = benzimidazole) nanosheets.[83] Zhao *et al.*[84] synthesized ultrathin NiCo bimetal-MOF nanosheets *via* ultrasonication exfoliation, showing an outstanding OER catalytic activity (overpotential of 250 mV at 10 mA $cm^{-2}$), much smaller than that of the bulk MOF counterpart (317 mV). In 2014, Xie *et al.*[85] prepared $CoSe_2$/DETA ultrathin

 

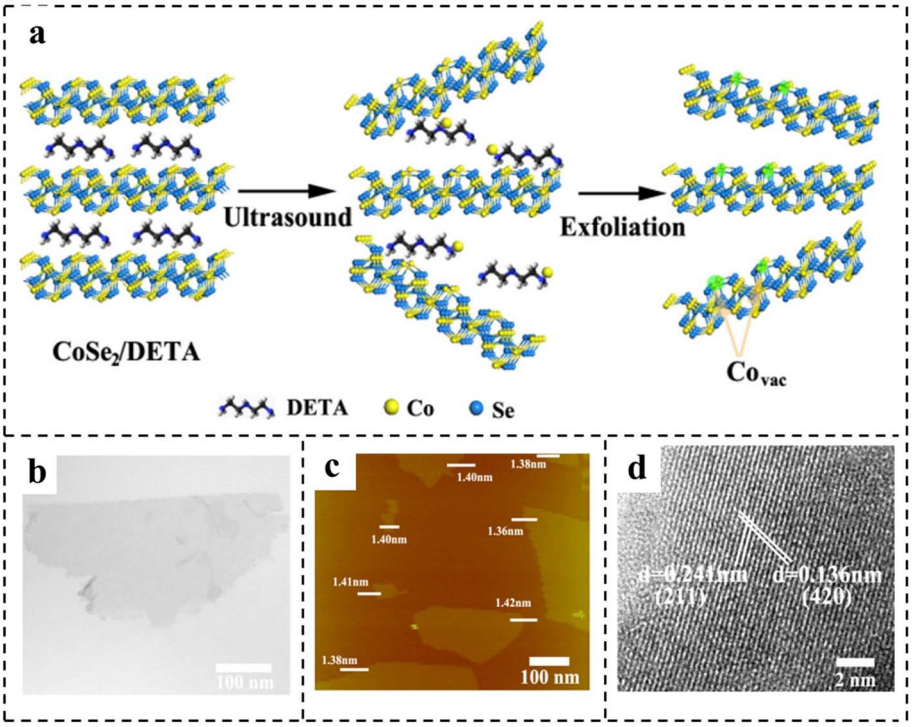


Fig. 6 (a) Schematic of the formation of vacancies in $CoSe_2$ ultrathin nanosheets. Characterization of $CoSe_2$ ultrathin nanosheets: (b) TEM image; (c) AFM image; (d) HRTEM image. Reproduced with permission from ref. 85. Copyright 2014, American Chemical Society.

layered nanosheets (about 1.4 nm) (Fig. 6b–d) by the ultrasonic stripping method (as shown in Fig. 6a). In the experiment, $CoSe_2$/DETA was dispersed in ethanol and ultrasonically treated with ice water for 12 h. Studies found that vacancy formation was closely related to the synthesis process. Ultrasonic treatment could enable DETA to separate Co atoms from the lattice due to the existence of coordination bonds between Co atoms and DETA and form Co vacancies, which could be used as active sites for effective adsorption of $H_2O$ molecules, thus significantly improving the catalytic performance of the OER. Subsequently, Kim *et al.*[86] prepared a series of TMD nanosheets ($MoS_2$, $WS_2$, $TaS_2$ and $TiS_2$) with about several hundred nanometers in size using a similar method and applied them in the HER. Although the ultrasonic stripping method is easy to operate, it also has some disadvantages, such as low yield and limited application range (it is generally only suitable for the structures with weak interlayer interaction).[87,88]

**3.1.4 Chemical stripping.** The ultrasonic stripping is only applicable to the materials with weak interlayer interaction. However, the interaction force of some materials in the vertical direction is very strong, and simple ultrasonic treatment cannot achieve efficient results. Therefore, the chemical stripping method is explored. Monolayer g-$C_3N_4$ nanosheets were prepared by the chemical exfoliation method.[89] During the exfoliation process, $H_2SO_4$ entered the interlayer of bulk g-$C_3N_4$, and a single layer of g-$C_3N_4$ nanosheets with a thickness of about 0.4 nm (Fig. 7b and c) and a radial size of several microns was obtained (Fig. 7a). The yield of the prepared g-$C_3N_4$ nanosheets was up to 60% using such a method, and the specific surface area of the obtained monolayer g-$C_3N_4$ nanosheets was about 205.8 $m^2\ g^{-1}$, which was about 50 times that of bulk g-$C_3N_4$ (4.3 $m^2\ g^{-1}$).

Song *et al.*[90] obtained MnDMS nanosheets from a flexible ligand 2,2-dimethylsuccinate and Mn ions. The MnDMS nanoparticles could be obtained by simple ultrasonication of a MnDMS crystal, which could then be exfoliated into ultrathin nanosheets by lithium-ion intercalation. Huang *et al.*[91] developed an electro-chemical/chemical exfoliation strategy to prepare ultrathin 2D Co-MOF nanosheets as an efficient OER electrocatalyst. Chemical exfoliation is also generally suitable for stripping bulk TMDs with organolithium compounds such as butyllithium (BuLi),[92,93] methyllithium (MeLi),[94] or lithium borohydride ($LiBH_4$)[95] as intercalation reagents (Fig. 8a–e). In these studies, Jin *et al.*[93] converted 2H–$MoS_2$ multilayered semiconducting nanostructures into 1T-$MoS_2$ polycrystalline nanosheets by soaking them in *n*-butyl lithium solution at room temperature for 6–48 hours (Fig. 8b). Due to the electron transfer of the embedded Li, the original triangular prismatic 2H–$MoS_2$ structure was destroyed, which was conducive to the octahedral coordination of Mo atoms, thus achieving the transition to the 1T phase. Then, by reacting the embedded lithium with excess water to produce hydrogen, the nanostructures were stripped away, thereby separating the two-dimensional nanosheets.

**3.1.5 Mechanical stripping.** Mechanical stripping is also a common method for preparing 2D layered nanomaterials. For the first time in 2004, Novoselov *et al.*[23] used the mechanical stripping method to successfully shed the high directional

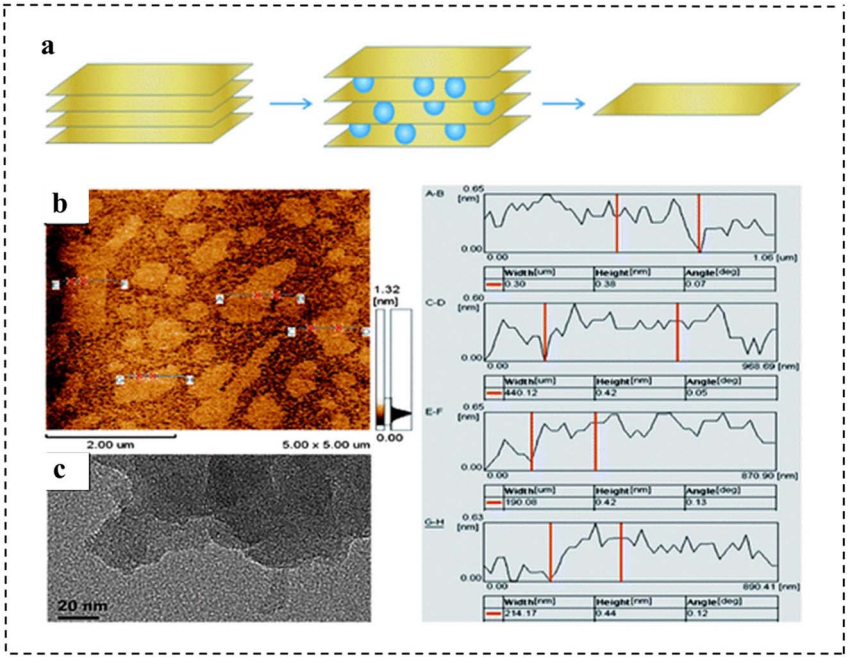


Fig. 7 (a) Illustration of the synthetic strategy of monolayer g-$C_3N_4$ nanosheets. (b) AFM images and (c) TEM images of the as-prepared monolayer g-$C_3N_4$ nanosheets. The right panel shows the height and width information of different nanosheets from the AFM images. Reproduced with permission from ref. 89. Copyright 2013, Royal Society of Chemistry.

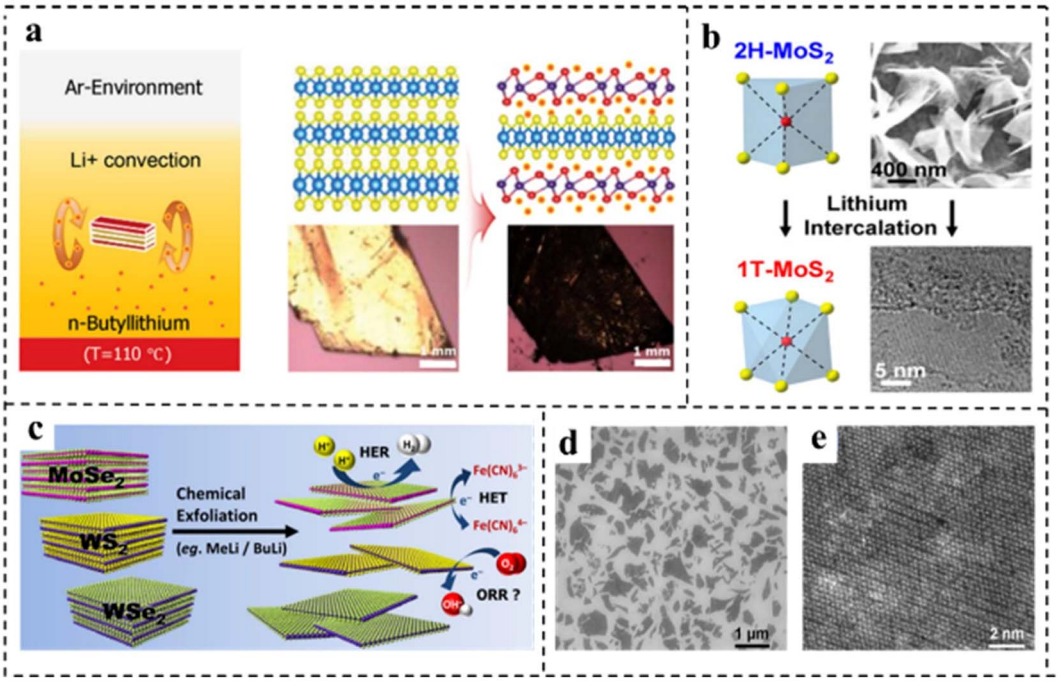


Fig. 8 (a) Illustration of the synthetic strategy and structure of vertical hetero-phase $MoTe_2$ (experimental setup for the $Li^+$-intercalation into a $MoTe_2$ single crystal, and the convectional flow of $Li^+$ ions was described by two brown arrows in *n*-butyllithium solution). Reproduced with permission from ref. 92. Copyright 2019, Wiley-VCH. (b) Illustration of the synthetic strategy of 1T-$MoS_2$. Reproduced with permission from ref. 93. Copyright 2013, American Chemical Society. (c) Illustration of the synthetic strategy of various chemically exfoliated TMDs ($MoSe_2$, $WS_2$, and $WSe_2$). Reproduced with permission from ref. 94. Copyright 2014, American Chemical Society. (d) SEM image of chemically exfoliated $MoS_2$ nanosheets deposited on $SiO_2$. (e) HRTEM image of chemically exfoliated $MoS_2$ with octahedral coordination (1T phase). Reproduced with permission from ref. 95. Copyright 2013, American Chemical Society.

 

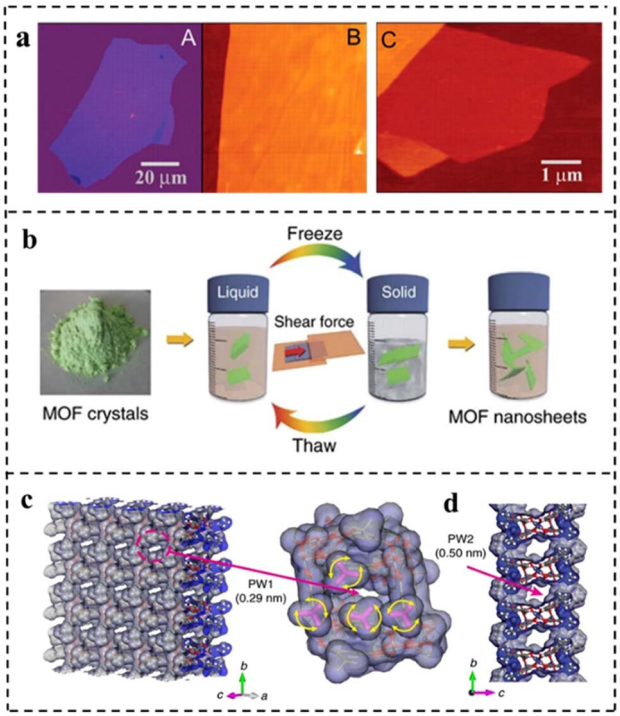


Fig. 9 (a) Graphene films: (A) photograph (in normal white light) of a relatively large multilayer graphene flake with a thickness of ~3 nm on top of an oxidized Si wafer. (B) AFM image of a 2 μm by 2 μm area of this flake near its edge. Colors: dark brown, $SiO_2$ surface; orange, 3 nm height above the $SiO_2$ surface. (C) AFM image of single-layer graphene. Colors: dark brown, $SiO_2$ surface; brown-red (central area), 0.8 nm height; yellow-brown (bottom left), 1.2 nm; orange (top left), 2.5 nm. Notice the folded part of the film near the bottom, which exhibited a differential height of ~0.4 nm. Reproduced with permission from ref. 23. Copyright 2004, The American Association for the Advancement of Science. (b) Schematic of freeze–thaw exfoliation of MAMS-1 crystals into dispersed nanosheets. (c) Tilted vertical view of the ab plane in the MAMS-1 monolayer featuring PW1 (amplified view of PW1 highlighted in magenta). (d) View along an axis of the MAMS-1 monolayer featuring PW2. Reproduced with permission from ref. 96. Copyright 2017, Springer Nature.

pyrolysis graphite and observed monolayer graphene. As shown in Fig. 9a, the graphene films were prepared by mechanical exfoliation (repeated peeling) of small mesas of highly oriented pyrolytic graphite. This approach was found to be highly reliable and enable the preparation of FLG (few-layer graphene) films up to 10 μm in size. Since then, a series of mechanical stripping methods have been developed, which use external or internal mechanical force to break the interaction between layers (such as van der Waals force, hydrogen bonding and π–π stacking). It is an effective method to obtain micron-sized and ultrathin 2D materials. Zhao *et al.*[96] reported a new mechanical stripping method based on a solvent lyophilization and thawing process. The crystal powder of a MOF (MAMS-1 (Mesh Adjustable Molecular Sieve, $Ni_8(5\text{-bbdc})_6(\mu\text{-OH})_4$)) was dispersed in hexane solution, which was then quickly frozen and thawed (Fig. 9b). The layers of MAMS-1 were held loosely together through van der Waals interactions which could be easily overwhelmed to afford nanosheets. At the same time, the nanosheet had two possible gas permeation pathways interconnected with each other. One pathway (PW1) was roughly perpendicular to the monolayer basal plane with a pore size of about 0.29 nm (Fig. 9c). The second pathway (PW2) with an aperture of about 0.50 nm was distributed along a direction parallel to the monolayer base plane (Fig. 9d). Due to the special structure of the gas channel and the small pore size of PW1, the gas could be discharged in the direction perpendicular to the monolayer base plane through the molecular sieve separation mechanism, so as to obtain lamellar AMS-1 nanosheets arranged in the direction perpendicular to the monolayer base plane. Due to the extreme volume variation between the solid and liquid phases of the hexane solvent, the resulting shear force was applied to the suspended crystals and promoted the formation of the peeled 2D nanosheets. The resulting nanosheet has an ultrathin thickness of a few atomic layers (about 4 nm) and a large transverse size (10.7 nm).

In 2010, a monolayer and small amount of $MoS_2$ were stripped on a $SiO_2$/Si substrate. Using a micromechanical stripping method widely used for preparing graphene samples, large pieces of $MoS_2$ were placed on a strip of tape, which was repeatedly folded and unfolded to separate single and multilayer $MoS_2$ films from the 2H–$MoS_2$ bulk crystal and then pressed the tape onto a silicon substrate covered with a $SiO_2$ layer. The measurements showed that exfoliation produced

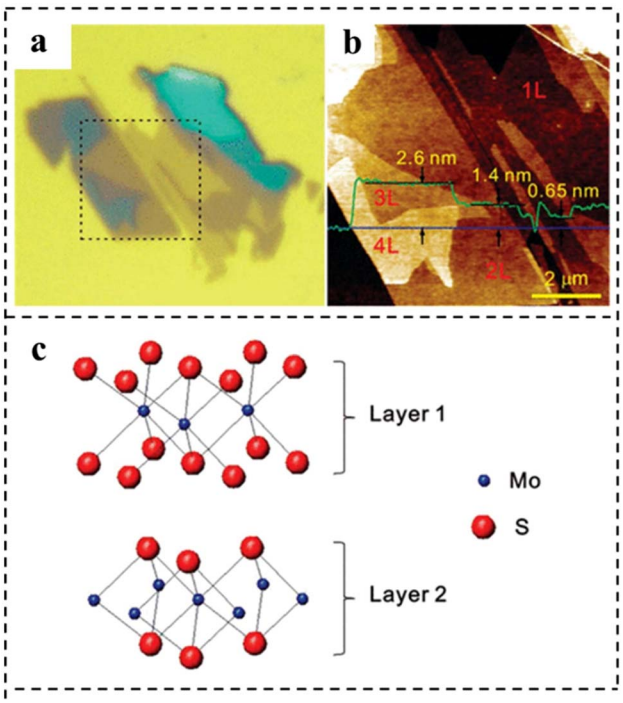


Fig. 10 (a) Optical micrograph of thin $MoS_2$ films deposited on the $SiO_2$/Si substrate. (b) AFM height image was taken for the 8 × 8 $\mu m^2$ area indicated by dotted lines in (a). The thickness of each layer is shown by the height profile (in green) taken along the blue line in the AFM image. (c) Schematic model of the $MoS_2$ bilayer structure. Reproduced with permission from ref. 97. Copyright 2010, American Chemical Society.

layers with a discrete number of these units. The measurements showed that exfoliation produced layers with a discrete number of these units. The AFM image showed that the thickness of monolayer $MoS_2$ was 0.6–0.7 nm, which was consistent with the layer spacing of monolayer $MoS_2$ (0.62 nm), and the films composed of $MoS_2$ showed a wide distribution in heights due to the stacking of layers (Fig. 10a–c).[97]

**3.1.6 Etching.** The chemical etching strategy is the main method to prepare MXenes, in which HF is widely used as the etching agent. The HF etching process was first used by Gogotsi[98] and co-workers in 2011 to directly etch Al from $Ti_3AlC_2$, through a simple displacement reaction. At the same time, HF and water molecules reacted with $Ti_3C_2$ to form surface terminal groups including –O, –OH, and –F. Later, Gogotsi *et al.* reported a series of MXenes obtained by HF etching, such as $Ti_2AlC$, $Ta_4AlC_3$, $(Ti_{0.5}Nb_{0.5})_2AlC$, $(V_{0.5}Cr_{0.5})_3AlC_2$, $Ti_3AlCN$,[99] $Ti_3C_2$, $Ta_4C_3$, TiNbC, $(V_{0.5}\ Cr_{0.5})_3C_2$, *etc.*[100] However, the use of F-containing reagents results in functional surface groups of the products containing F, which limits their application in electrocatalysis. Later developed electrochemical etching is an efficient and safe alternative to MXenes. Yang *et al.*[101] prepared monolayer or bilayer $Ti_3C_2T_x$ by electrochemically etching $Ti_3AlC_2$ with 1 mol $L^{-1}$ $NH_4Cl$ and 0.2 mol $L^{-1}$ tetramethylammonium hydroxide as electrolytes (as shown in Fig. 11a). In this method, chloride ions were able to rapidly etch the anode Al and break the Ti–Al bond. The subsequent intercalation of $NH_4OH$ played a key role in opening the edges of the etched anode and facilitating etching below the surface. The structural changes during the etching/delamination process were clearly revealed by X-ray diffraction (XRD) patterns (Fig. 11b). Due to the introduction of functional groups and the intercalation of $NH_4OH$ molecules between the $Ti_3C_2T_x$ layers, the (002) peak of $Ti_3AlC_2$ moved to a lower angle (9.888° to 7.888°), corresponding to an increase in the *c* lattice parameter from 18.0 to 22.6 Å. At the same time, TEM (Fig. 11c and d) images showed enlarged interlayer distances, which agreed well with the XRD results. $Ti_3C_2T_x$ nanosheets with high yield (>90%) can be obtained by this electrochemical etching method, which was much higher than the yield (45%) of $Ti_3C_2T_x$ nanosheets using HF as the etching agent. The nanosheets obtained by this method had a large spectral surface area and excellent hydrophilicity, which had competitive advantages in electrocatalysis. Liu *et al.*[102] using plasma etching of CoFe-LDHs grown on nickel foam found that at the same current density, the plasma-etched CoFe-LDHs (optimized sample) had a lower overpotential (95 mV) than the original CoFe-LDHs. This indicated that HER catalytic activity was significantly improved by ion etching.

### 3.2 Bottom-up

Although top-down approaches facilitate the preparation of 2D nanomaterials with specific properties and provide low-cost products using direct methods, these approaches still have limitations for the practical application of 2D nanomaterials. These problems include formation of unstable nanosheets, inability to control the number of layers, limitation of layered materials, low yield of products, and frequent breakage and restacking of stripped nanosheets. Unlike the top-down approach, the bottom-up synthesis method enables the synthesis of different ultrathin nanosheets by controlling the growth direction or inhibiting the chemical synthesis of inter-layer interactions during the synthesis process. It has the advantages of high preparation yield, controllable thickness, large transverse size

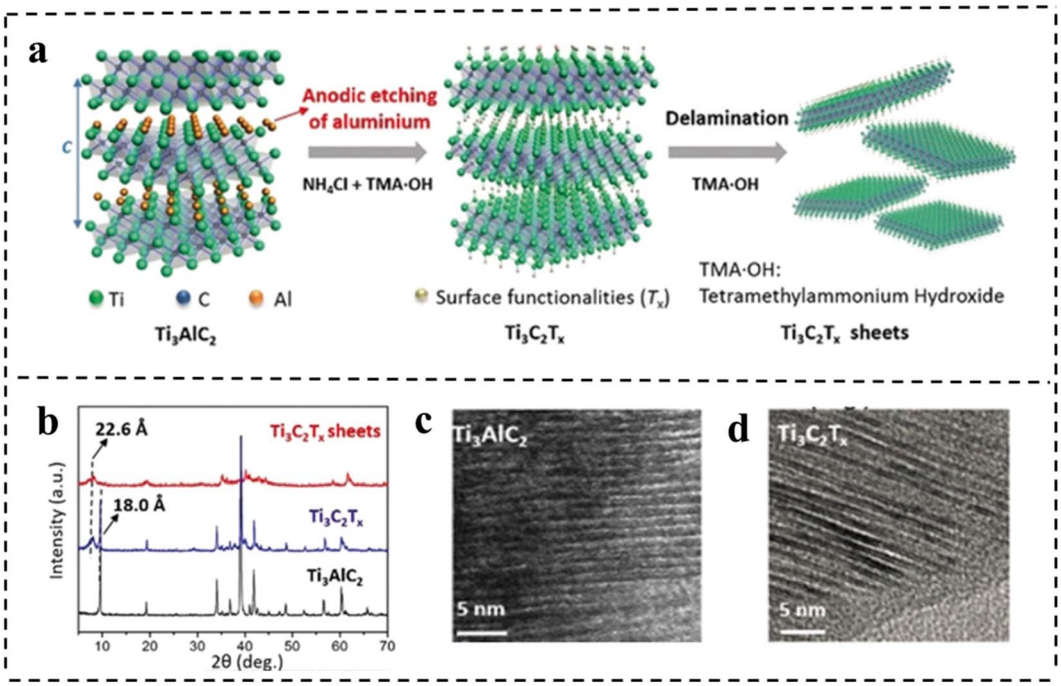


Fig. 11 (a) Schematic of the etching and delamination process of bulk $Ti_3AlC_2$. (b) XRD patterns of $Ti_3AlC_2$ and $Ti_3C_2T_x$. HRTEM images of (c) $Ti_3AlC_2$ and (d) $Ti_3C_2T_x$, respectively. Reproduced with permission from ref. 101. Copyright 2018, Wiley-VCH.

 

and good dispersion for the synthesized 2D nanomaterials. Common bottom-up synthesis methods include solvothermal synthesis, surfactant-assisted synthesis, chemical vapor deposition, inorganic–organic additive synthesis, *etc.*

**3.2.1 Solvothermal synthesis.** Solution thermal synthesis is one of the most common methods for preparing 2D materials. The relative growth rate in different directions can be modified by adjusting reaction conditions (such as solvent, temperature and reaction time). In this way, products with different sizes, shapes and even crystal structures can be obtained. When the growth rate of the edge is much faster than that of the vertical direction, the surfaces with a lower growth rate are easily exposed, which makes it possible to construct 2D nanosheets.[103] In 2005, Rao *et al.*[104] prepared Mg–Al hydrotalcite by hydrothermal synthesis. Wang's group[105] prepared NiMn-LDHs by a simple one-step hydrothermal method. And Zhao *et al.*[106] synthesized 2D Zr/Hf MOF nanosheets named NUS-8 composed of $Zr_6O_4(OH)_4$ or $Hf_6O_4(OH)_4$ clusters and 1,3,5-benzenetribenzoate directly *via* a heterogeneous modulated hydrothermal approach in the absence of surfactants. Structural analyses confirmed the 2D layered structure of NUS-8 with uniform porosity and highly accessible Lewis acid sites suitable for heterogeneous catalysis. Li *et al.*[107] prepared a series of binary Ni-M-MOF (M = Fe, Al, Co, Mn, Zn and Cd) ultrathin nanosheets in a mixture of *N*,*N*-dimethylacetamide (DMA) and water using a simple solvothermal synthesis method and successfully applied them to OER catalysis (Fig. 12a). These ultrathin bimetallic Ni–M–MOF NSs were prepared by a one-step solvothermal reaction, and the key to success was the proper use of the DMA/$H_2O$ mixture. Amorphous nanoflowers with nanoparticles were generated using only water as solvent, and porous and fluffy powders were generated using only DMA as solvent (Fig. 12b). During the solvothermal process, DMA dissolved the organic ligands and avoided the formation of nanoparticles. Meanwhile, water not only occupied the metal coordination sites on the surface and restricted the growth of coordination polymers, but also acted as a good exfoliator. The synthesized material was well exposed to the active site and had fast electron transfer ability. The mixed metal synergy and unique coordination environment around the active site enhanced the catalytic activity. Among them, ultra-thin Ni–Fe–MOF NSs (Fig. 12c) showed highly enhanced activity and durability for the OER. Eng *et al.*[108] proposed a universal synthesis approach for TMDs based on the solvothermal method using only a common tetrathio-metallate precursor, in which the composition (Mo and W), phase (semiconductor and

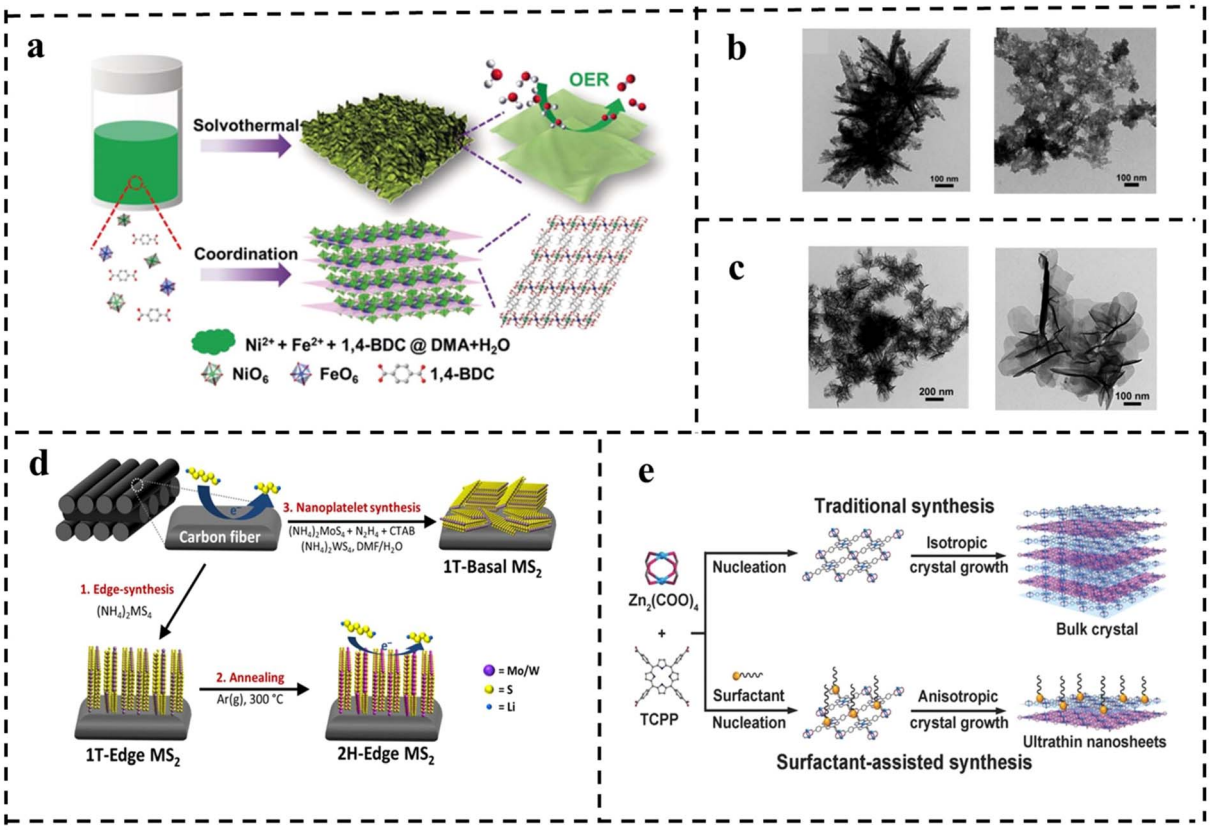


Fig. 12 (a) Schematic of the synthetic process for the ultrathin metal–organic framework nanosheets and their utilization for the OER. TEM images of (b) with water as solvent only and with DMAC as reaction solvent only and (c) ultra-thin NiFe-MOF NSs. Reproduced with permission from ref. 107. Copyright 2019, Wiley-VCH. (d) Schematic of structured synthesis of TMDs ($MS_2$, M = Mo/W) on carbon cloth. Reproduced with permission from ref. 108. Copyright 2019, Elsevier. (e) Schematic of the synthesis of Zn-TCPP. Reproduced with permission from ref. 109. Copyright 2015, Wiley-VCH.

metal), and morphology (edge and base plane orientation) could be controlled (Fig. 12d).

The solvothermal method has the advantages of being easy to operate (one-step synthesis) and easy to scale (gram-scale has been achieved in some cases), and is a no-addition process. However, it is only sometimes applicable to different situations, and direct solvothermal synthesis largely depends on the proper selection of solvents and reaction conditions.

**3.2.2 Surfactant-assisted synthesis.** The surfactant assisted synthesis method is convenient and flexible, providing an excellent solution to the problem of bottom-up synthesis of 2D MOF nanosheets in the liquid phase. Surfactants have been widely used to control the growth of nanocrystals because they can selectively adhere to special small planes of nanocrystals. It can also design and synthesize ultra-thin MOF nanosheets with other functional ligands. Polyvinylpyrrolidone (PVP) is one of the most commonly used surfactants and can selectively regulate the vertical overgrowth of MOFs. For example, in 2015, Zhao *et al.*[109] reported a simple surfactant assisted synthesis method for the preparation of ultra-thin 2D M-TCPP (M = Zn, Cu, Cd or Co, TCPP = tetra (4-carboxyl phenyl) porphyrin) nanosheets (Fig. 12e). In the experiment, with TCPP as the organic ligand and Zn, Cu, Cd or Co as the nodes, in the presence of surfactant PVP, PVP can selectively adhere to the surface of MOFs, restricting the growth of MOFs along the vertical direction, resulting in the anisotropic growth of MOFs. Thus, a series of stable ultra-thin 2D nanosheets with thickness below 10 nm were obtained.

**3.2.3 Chemical vapor deposition (CVD).** The CVD method is a bottom-up method to produce high quality and high-performance 2D nanomaterials. CVD is a technique where a solid material is deposited from a vapor by some chemical reaction occurring on or in the vicinity of a normally heated substrate surface. The CVD method has some advantages: it uses source material that flows from an external tank into the process chamber and can be refilled without contaminating the growth environment; it does not require a high vacuum; it can typically process larger volumes of the substrate than evaporation.[110,111] Chen *et al.*[112] synthesized high-quality single-layer $MoS_2$ with mm grade size by the CVD method. The size of the monolayer crystals was about 2.5 mm, and the carrier mobility was up to 95 $cm^2 V^{-1} s$ at room temperature, which can be used for the electrocatalytic HER, OER and energy storage. Kumar

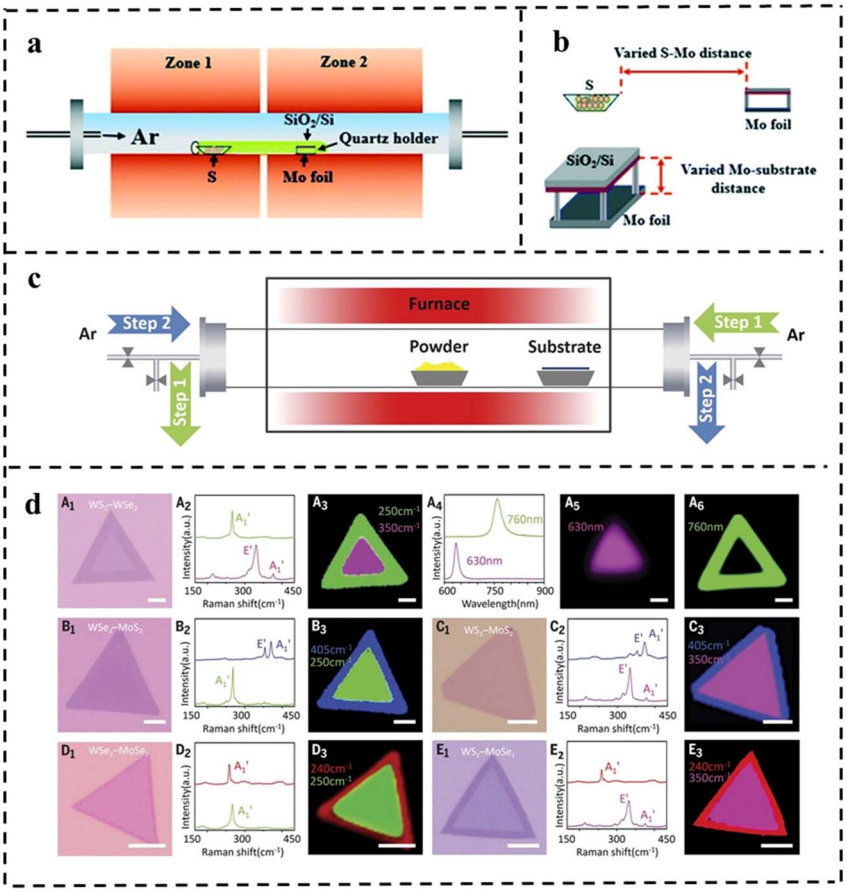


Fig. 13 (a) The sketch of the CVD system for the growth of $MoS_2$ flakes. (b) Schematic diagram of the varied distance between Mo foil and the S/growth substrate. Reproduced with permission from ref. 114. Copyright 2021, Royal Society of Chemistry. (c) Schematic diagram of the modified CVD system with a reversible Ar flow for the epitaxial growth of the lateral TMD heterostructures. (d) Optical microscopy images for the grown various 2D NSs with lateral heterostructures using the setup and their corresponding characterization. Reproduced with permission from ref. 115. Copyright 2017, The American Association for the Advancement of Science.

 

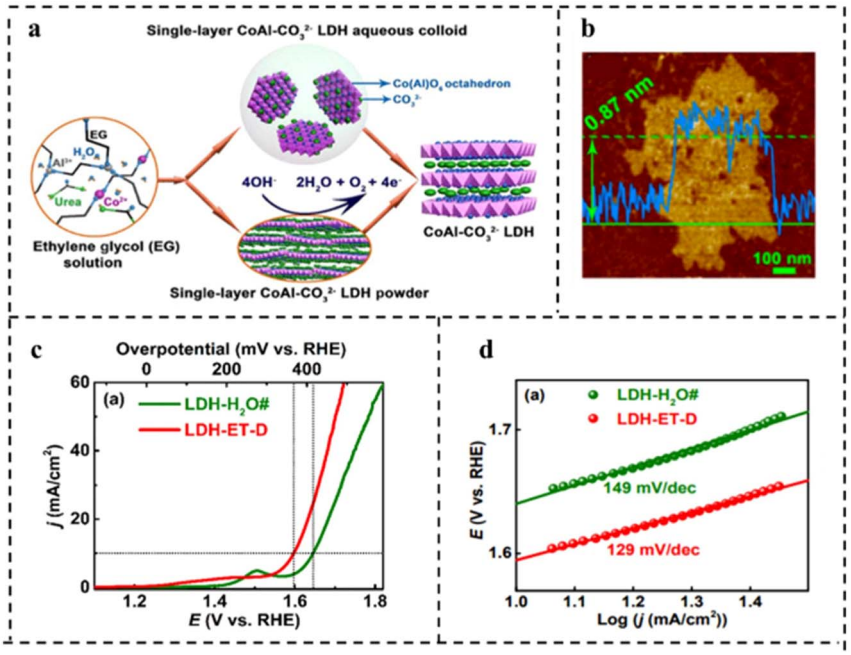


Fig. 14 (a) Schematic diagram of synthesis of water-dispersible single-layer CoAl–$CO_3^{2-}$ LDH. (b) AFM image of single-layer CoAl–$CO_3^{2-}$ LDH. (c) Polarization curves in $O_2$-saturated 1 M KOH at a scan rate of 0.5 mV $s^{-1}$. (d) Tafel plots corresponding to (c). Reproduced with permission from ref. 116. Copyright 2017, American Chemical Society.

*et al.*[113] also used the same method to prepare $MoS_2$ nanosheets, and electrochemical tests found that $MoS_2$ nanosheets had good HER catalytic activity, and the use of visible light in electrocatalysis would almost double its catalytic activity. Recently, Chen *et al.*[114] synthesized 2D $MoS_2$ flakes by the confined space CVD method (Fig. 13a). It was found that the 2D $MoS_2$ dimension could be controlled by controlling the amount of sulfur powder, the growth temperature and the distance between the substrate S powder and the Mo foil (Fig. 13b).

The improved step-by-step CVD synthesis could fabricate multiple heterojunctions. In general, the lateral heterostructures of the two different TMD monolayers are fragile and may not survive the multi-step growth process. In 2017, Zhang *et al.*[115] proposed a novel step-by-step synthesis strategy that successfully solved this problem. Various in-plane 2D TMD nanostructures were grown by reversing the gas flow direction. Firstly, monolayer TMD NSs were grown on a substrate by the CVD method. During the sequential growth process, the original long monolayer was placed downstream of the argon gas flow, which reversed the flow during the temperature change, thus cooling the existing monolayer TMD material and preventing undesirable thermal degradation from occurring. Also, the reverse argon flow suppressed uncontrolled nucleation prior to the sequential growth step (Fig. 13c). This effective CVD technique can produce $WSe_2$–$MoS_2$ and multiple heterojunctions ($WS_2$–$WSe_2$–$MoS_2$ and $WS_2$–$MoSe_2$–$WSe_2$, Fig. 13d).

**3.2.4 Additive-assisted synthesis.** In 2017, Yu *et al.*[116] synthesized monolayer $CO_3^{2-}$ intercalated CoAl-LDH with a thickness of about 0.85 nm using ethylene glycol as solvent (Fig. 14a and b), in which ethylene glycol had strong chelation with metal ions, which slowed down the nucleation and growth of LDH crystals, and their adsorption on the monolayer LDH surface. The growth of LDH along the *C*-axis was prevented, which could form monolayer LDH. At the same time, the material had excellent stability and could retain its original shape after five months in water. Compared with the monolayer LDHs synthesized directly with water as a solvent (LDH-$H_2O$), the single-layer CoAl-LDH synthesized by this method had better electrocatalytic OER performance, which required an applied overpotential as low as 367 mV at 10 mA $cm^{-2}$ with a lower Tafel slope (129 mV $dec^{-1}$), whereas LDH-$H_2O$ required 415 mV at 10 mA $cm^{-2}$ with a Tafel slope of 149 mV $dec^{-1}$ (Fig. 14c and d).

## 4. Activation strategies

In this section, we will focus on the recent development of 2D bifunctional nanocatalysts with both HER and OER activity in the field of full water splitting. And we will discuss and summarize some typical strategies for enhancing bifunctional activities, including doping, nanocomposite construction, interface formation, defect engineering, morphology modulation and so on. The structure–activity relationships will also be discussed with the aim of providing guidance in designing novel 2D bifunctional electrocatalysts. The recent research advancements in 2D bifunctional nanocatalysts for full water splitting are comprehensively summarized in Table 1.

### 4.1 Doping

Doping can tailor the band structure, valence state of the active site, charge redistribution, and the adsorption and desorption

Table 1 Comparison of representative bifunctional electrocatalysts for overall water splitting

| | | | | $\eta_{10}$ | | | Tafel slope | | |
|---|---|---|---|---|---|---|---|---|---|
| | Catalyst | Synthesis method | Electrolyte | HER | OER | Overall WE | HER | OER | Ref. |
| Activation strategies | NiVRu-LDH | One-pot hydrothermal | 1.0 M KOH | 12 mV | 190 mV | 1.42 V | 40 mV $dec^{-1}$ | 83 mV $dec^{-1}$ | 118 |
| | NiVIr-LDH | | | 47 mV | 180 mV | | 107 mV $dec^{-1}$ | 38 mV $dec^{-1}$ | |
| | Ni–$MoSe_2$@$Ti_2NTx$ | Hydrothermal | 1.0 M KOH | 92 mV | 270 mv ($\eta_{50}$) | 1.59 V | 79.7 mV $dec^{-1}$ | 81.1 mV $dec^{-1}$ | 119 |
| Nanocomposite construction | NiFe LDH-NS@DG10 | Stripping | 1.0 M KOH | 300 mV | 210 mV | 1.5 V | 110 mV $dec^{-1}$ | 52 mV $dec^{-1}$ | 125 |
| | $Ni_3S_2$/VG@NiCo LDHs | Electrodeposition | 1.0 M KOH | 120 mV | 320 mV ($\eta_{100}$) | 1.66 V | 87 mV $dec^{-1}$ | 97 mV $dec^{-1}$ | 126 |
| | CoFe@NiFe/NF | Hydrothermal electrodeposition | 1.0 M KOH | 240 mV | 190 mV | 1.59 V | 88.88 mV $dec^{-1}$ | 45.7 mV $dec^{-1}$ | 127 |
| | Ir/g-$C_3N_4$/NG | Solvothermal | 1.0 M KOH | 22 mV | 300 mV | 1.56 V | 22 mV $dec^{-1}$ | 72.8 mV $dec^{-1}$ | 128 |
| | g-$C_3N_4$/$CeO_2$/$Fe_3O_4$ | Coprecipitation | 1.0 M KOH | 310 mV | 400 mV | 1.94 V | 102 mV $dec^{-1}$ | 74 mV $dec^{-1}$ | 129 |
| | CoP/$Ti_3C_2$ MXene | *In situ* phosphorylation | 1.0 M KOH | 102 mV | 280 mV | 1.58 V | 68.7 mV $dec^{-1}$ | 95.4 mV $dec^{-1}$ | 131 |
| | NFPS@MXene | Self-assemble | 1.0 M KOH | 196 mV | 282 mV | 1.65 V | 114 mV $dec^{-1}$ | 36.5 mV $dec^{-1}$ | 132 |
| | $Ni_3S_2$@$MoS_2$/FeOOH | Electrodeposited | 1.0 M KOH | 95 mV | 234 mV | 1.57 V | 85 mV $dec^{-1}$ | 49 mV $dec^{-1}$ | 134 |
| | LSC/K–$MoSe_2$ | Sol–gel molten-metal-assisted | 1.0 M KOH | 128 mV | 230 mV | 1.59 V | 45 mV $dec^{-1}$ | 79 mV $dec^{-1}$ | 135 |
| Interface formation | ZIF/Ni–B@NF | Room-temperature boronization | 1.0 M KOH | 67 mV | 234 mV | 1.54 V | 108 mV $dec^{-1}$ | 76 mV $dec^{-1}$ | 140 |
| | $MoSe_2$–$Cu_2S$ (NHSs) | Defect passivated colloidal | 1.0 M KOH | 350 mV | 264 mV | — | 110 mV $dec^{-1}$ | 63 mV $dec^{-1}$ | 141 |
| | $Ni_{0.85}Se$–$MoSe_2$ | Solvothermal hydrothermal | 1.0 M KOH | 108 mV | 380 mV | 1.70 V | 77 mV $dec^{-1}$ | — | 142 |
| | $Ni_{0.75}Se$ | Solvothermal hydrothermal | 1.0 M KOH | 221 mV | 340 mV | | 172 mV $dec^{-1}$ | — | |
| Defect engineering | P–V–NiFe LDH NSA | Cation doping plasma reduction | 1.0 M KOH | 19 mV | 29 5 mV ($\eta_{100}$) | 1.43 V | 38 mv $dec^{-1}$ | 56 mV $dec^{-1}$ | 147 |
| | $MoS_2$/$NiS_2$ | Hydrothermal | 1.0 M KOH | 62 mV | 278 mV | 1.59 V | 50.1 mV $dec^{-1}$ | 91.7 mv $dec^{-1}$ | 148 |
| Morphology modulation | $CoSe_2$ spheres | Hydrothermal | 1.0 M KOH | — | 325 mV | — | — | 80 mV $dec^{-1}$ | 152 |
| | | | 0.5 M $H_2SO_4$ | 167 mV | — | — | 38 mV $dec^{-1}$ | — | |
| | NiFe-MOF | One-step chemical bath deposition | 0.1 M KOH | 134 mV | 240 mV | 1.55 V | — | 34 mV $dec^{-1}$ | 153 |
| | NiFe (dobpdc) | Hydrothermal | 1.0 M KOH | 113 mV | 207 mV | 1.59 V | 69 mV $dec^{-1}$ | 36 mV $dec^{-1}$ | 154 |
| | Cu@NiFeLDH | Electrodeposition | 1.0 M KOH | 116 mV | 199 mV | 1.54 V | 58.9 mV $dec^{-1}$ | 27.8 mV $dec^{-1}$ | 155 |

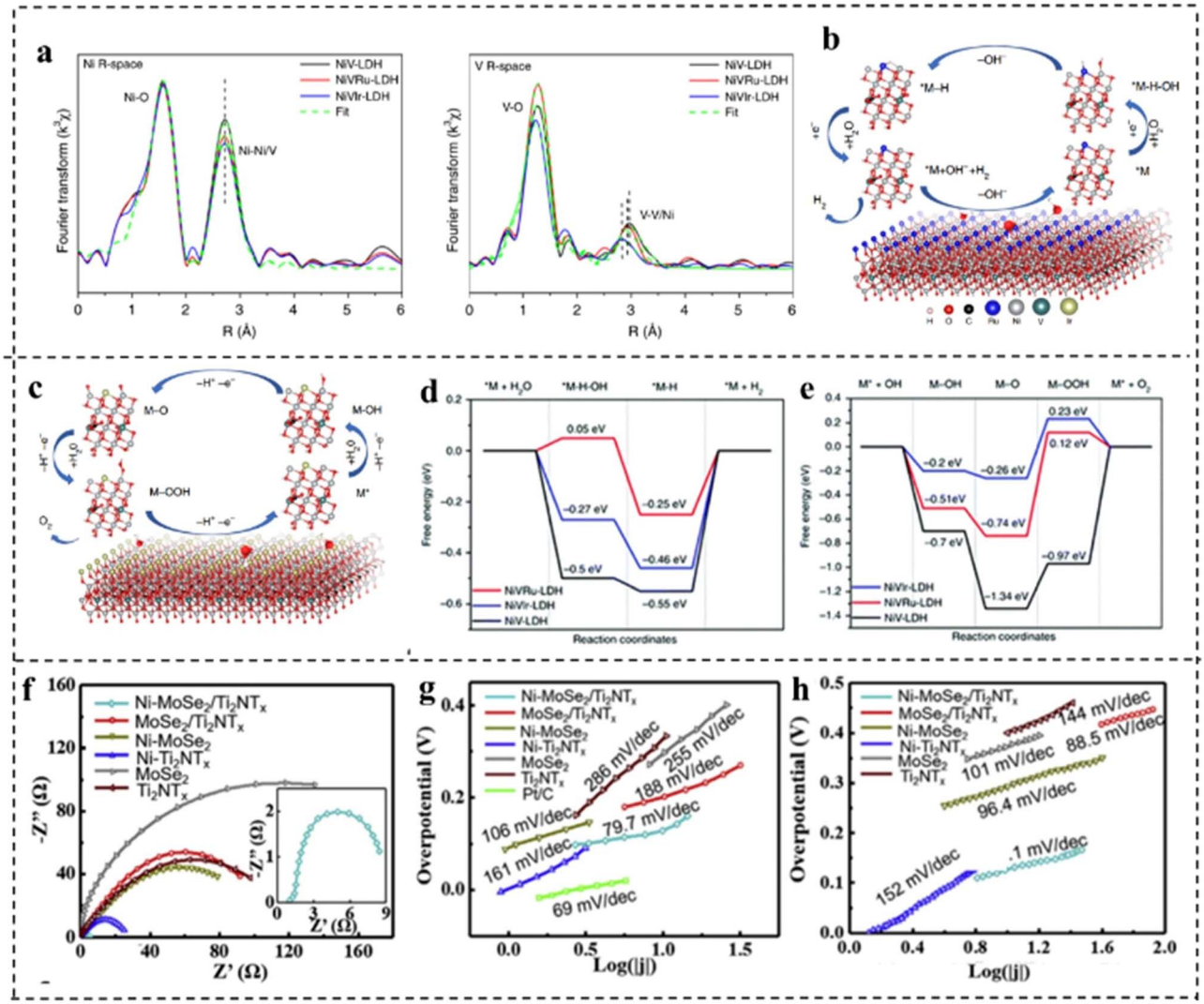


Fig. 15 (a) Ni and d V K-edge extended XANES oscillation functions $k^3\chi$ (k). (b) The atomic model of NiVRu-LDH and the proposed HER pathway. (c) The atomic model of NiVIr-LDH and the proposed OER pathway. (d) The free energy diagram of the HER and (e) OER on the NiV-LDH, NiVRu-LDH, and NiVIr-LDH catalysts. Reproduced with permission from ref. 118. Copyright 2019, Springer Nature. (f) The Nyquist plots and Tafel plots of HER performance (g) and OER performance (h) of Ni–$MoSe_2$@$Ti_2NT_x$ and other control materials. Reproduced with permission from ref. 119. Copyright 2020, Elsevier.

behaviors of reactants, intermediates and products, which facilitates $H_2$ and $O_2$ evolution.[117]

Xing *et al.*[118] synthesized NiV-LDH, NiVRu-LDH, and NiVIr-LDH by a simple one-step hydrothermal method and found that doping Ru or Ir in self-supported NiV-LDH could induce the V vacancy which was verified by Raman and X-ray absorption fine structure (XAFS) as shown in Fig. 15a. DFT calculations showed that Ru and Ir doping in NiV-LDH could optimize the adsorption energy of intermediates during the HER process, while accelerating the OER kinetic process as shown in Fig. 15b–e. Therefore, the NiVIr-LDH||NiVRu-LDH electrolyzer showed excellent catalytic activity which could provide a current density of 10 mA $cm^{-2}$ with only 1.42 V, much smaller than that of $RuO_2$||Pt/C.

Doping transition metals can also improve the electrical conductivity and stability of catalysts. For example, Zong *et al.*[119] synthesized Ni doped $MoSe_2$@$Ti_2NT_x$. The study revealed that Ni doped $MoSe_2$ had improved HER properties as Ni doping generated numerous hydrolysis sites and decreased the energy barrier required for overall water splitting. The replacement of Ni atoms with Mo in $MoSe_2$ also produced a catalyst with semiconducting properties, thus enhancing its electrical conductivity (Fig. 15f). For the HER, Ni–$MoSe_2$@$Ti_2NT_x$ showed an overpotential of 92 mV at 10 mA $cm^{-2}$ and a Tafel slope of only 79.7 mV $dec^{-1}$as compared to $MoSe_2$@$Ti_2NT_x$ ($\eta_{10}$: 139 mV and Tafel slope: 118 mV $dec^{-1}$), revealing that Ni doping profoundly elevated HER activity (Fig. 15g). For the OER, Ni–$MoSe_2$@$Ti_2NT_x$ revealed an $\eta_{50}$ of 270 mV and a Tafel slope of 81.1 mV $dec^{-1}$ as compared to $MoSe_2$@$Ti_2NT_x$ ($\eta_{50}$: 328 mV and Tafel slope: 96.4 mV $dec^{-1}$) (Fig. 15h). Due to the Ni doping improved HER and OER performance in alkaline media, Ni–$MoSe_2$@$Ti_2NT_x$ was utilized as both the anode and the cathode, which exhibited

a small voltage of 1.59 V to afford a current density of 10 mA $cm^{-2}$.

Although doping is one of the good strategies to improve the catalytic performance of 2D catalysts, there are still some limitations: the site and density of doping cannot be controlled precisely through currently developed synthesis techniques, which results in difficulty in fine-tuning the activity of electrocatalysts.

### 4.2 Nanocomposite construction

Constructing a 2D composite catalyst can enhance the water electrolysis efficiency of bifunctional catalysts.[120,121] The heterostructures usually comprise two or more different components, possibly integrating the merits and overcoming the disadvantages of the individual ones.[122,123] Hybridization of catalytically active components with highly conductive substrate materials to form composites is a widely used method that can synergistically achieve optimized electronic structures, abundant active sites, and improved operational stability,[124] and the selection of materials that can have a synergistic effect with existing materials is the difficulty of this strategy. This section summarizes the research advances in 2D materials including LDH, g-$C_3N_4$, MXene and TMD hybridizing with other components to construct bifunctional catalysts for overall water splitting in recent years.

2D carbonaceous materials (*e.g.*, graphene) with a large surface area and outstanding electrical conductivity have been considered ideal substrates for anchoring electrocatalysts to achieve enhanced activity. Yao's group[125] reported a highly efficient bifunctional catalyst based on strongly coupled stripped NiFe-LDH nanosheets and defective graphene (DG) (Fig. 16a). The catalyst showed high electrocatalytic activity for the OER, with an $\eta_{10}$ of 210 mV and a Tafel slope of 52 mV $dec^{-1}$ under alkaline conditions. The excellent OER and HER activities of the prepared NiFe LDH-NS@DG10 catalysts were due to the more efficient anchoring sites on DG brought about by the defects, which resulted in the direct and strong coupling of transition metal atoms (Ni and Fe) on 2D NiFe-LDH nanolayers. DFT calculations demonstrated that the separation and redistribution of electrons and holes on DG and NiFe LDH were achieved through the combination of DG and NiFe LDH (Fig. 16b and c). The high density of electrons on DG elevated the HER, while the high density of holes on NiFe LDH enhanced the OER. The Han, s group[126] reported a bifunctional electrocatalyst consisting of $Ni_3S_2$ as the template, vertical graphene (VG) as the bridging material, and NiCo-LDH nanosheets as the active catalyst, as shown in Fig. 16d–f. It is found that the VG bridging between NiCo-LDH and $Ni_3S_2$ enabled fast charge-transfer and a high density of active sites, resulting in improved electrical conductivity, intrinsic activity, and electrochemical stability. The hybrid $Ni_3S_2$/VG@NiCo LDH catalyst exhibited excellent activity in alkaline solution for both the OER and the HER. In addition, the hybrid catalyst possessed superior stability with 99% retention of voltage upon a continued

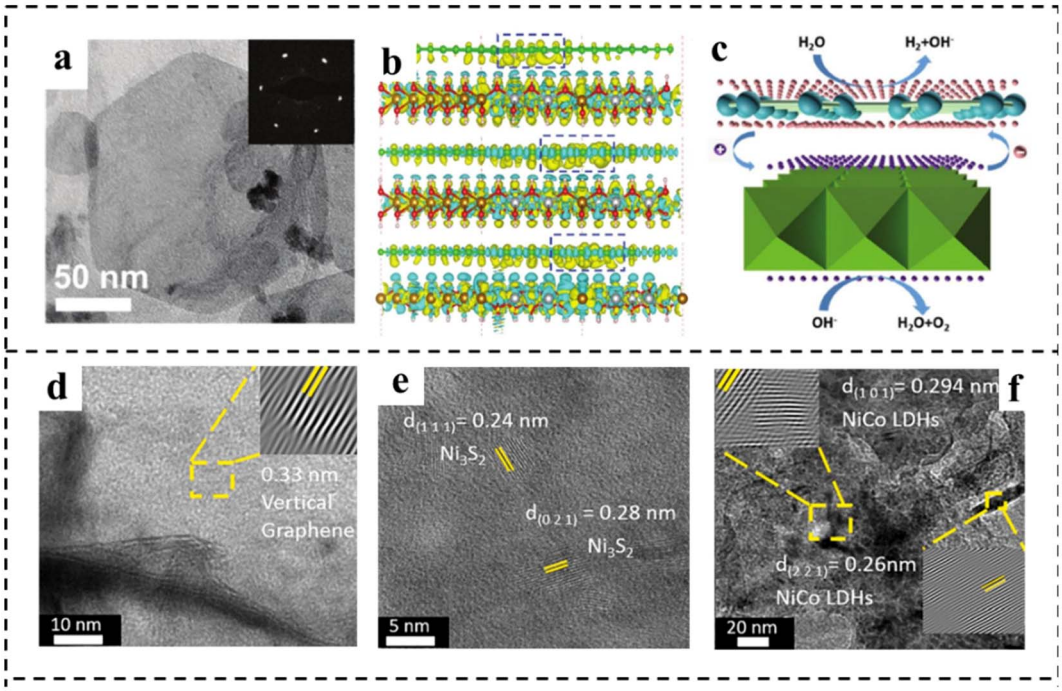


Fig. 16 (a) TEM image of typical exfoliated LDH-NS anchored on DG with the corresponding selected area diffraction pattern (inset). (b) The side views of the3D charge density difference plot for the interfaces between defective graphene sheets (DG-5, DG-585, or DG-5775). Yellow and cyan isosurfaces represent charge accumulation, and green, brown, silver, and red balls represent C, Fe, Ni, and O atoms, respectively. (c) Schematic illustration of NiFe LDH-NS@DG10 for overall water splitting. The pink and purple spheres represent electrons and holes, respectively. Reproduced with permission from ref. 125. Copyright 2017, Wiley-VCH. (d–f) HRTEM images of VG, $Ni_3S_2$, and NiCo LDHs. Reproduced with permission from ref. 126. Copyright 2021, Elsevier.

 

current density of 10 mA $cm^{-2}$ for over 24 h. Similarly, Shi and coworkers[127] prepared a novel CoFe-LDH@NiFe-LDH core–shell architecture on NF through a facile hydrothermal and electrodeposition method. The formed CoFe-LDH@NiFe-LDH core–shell architectures featured a 3D interconnected porous structure, which provided abundantly accessible active sites and contact areas with electrolytes. In addition, the strong electronic interaction between CoFe-LDH and NiFe-LDH not only promoted fast charge transfer at the interface, but also synergistically optimized the binding energies of the reaction intermediates, thus accelerating the reaction kinetics and enhancing the electrocatalytic efficiency. The resulting CoFe@NiFe/NF electrode architectures exhibited excellent activities and stabilities for the OER and HER. Furthermore, an efficient and stable alkaline electrolyzer using CoFe@NiFe/NF as both the cathode and anode achieved a voltage of 1.59 V at 10 mA $cm^{-2}$.

The construction of a composite can also solve the problems of poor conductivity and the lack of redox sites of graphitic carbon nitride (g-$C_3N_4$). Jiang *et al.*[128] reported nitrogen-doped graphene (NG) chemically coupled with g-$C_3N_4$ to form $C_3N_4$/NG layers composited with monodispersed Ir nanoparticles. The $C_3N_4$/NG layers facilitated the kinetics of overall electrochemical water splitting: firstly, due to the presence of pyridine N in g-$C_3N_4$, the nearby C atoms with $SP^2$ hybrid has a high positive charge density, which is conducive to the adsorption of the reactant and the charge transfer between the reaction species and the catalyst surface, thus improving the OER performance. Additionally, $C_3N_4$/NG delivered high HER performance owing to its moderate adsorption–desorption ability for hydrogen, thus accelerating the kinetics of full water splitting. Moreover, g-$C_3N_4$ was helpful to the dispersion of active materials without aggregation, thereby exposing the active sites. Rashid *et al.*[129] reported the first ternary composite based on g-$C_3N_4$, which consisted of g-$C_3N_4$, $CeO_2$ and $Fe_3O_4$, showing an excellent and durable bifunctional catalytic activity for the OER and HER in the alkaline medium owing to the synergetic effects between the three ingredients.

MXene has high conductivity, which can afford the rapid transfer of electrons, and as a result it is often used as a highly conductive substrate to improve the activity of catalysts.[130] For example, Yan and his group[131] reported a general approach to synthesize CoP/$Ti_3C_2$ MXene on $Ti_3C_2$ MXene nanosheets. In the CoP/$Ti_3C_2$ MXene hybrid, $Ti_3C_2$ MXene as a highly conductive substrate not only facilitated rapid electron transfer, but also prevented the aggregation of CoP nanoarrays. Meanwhile, CoP nanoarrays could prevent restacking of MXene nanosheets. Especially, the strong interactions between CoP and $Ti_3C_2$ MXene endowed the CoP/$Ti_3C_2$ MXene composite with exceptional catalytic activities and stabilities toward the HER at all pH values. Meanwhile, CoP/$Ti_3C_2$ MXene also exhibited superior OER performance in alkaline electrolyte. The CoP/$Ti_3C_2$ MXene even outperformed the commercial Pt/C||$IrO_2$ couple for overall water splitting under alkaline conditions. Du *et al.*[132] synthesized a novel $Ni_xFe_{1-x}$ $PS_3$/MXene (NFPS/MXene) hybrid through a facile self-assembly process of LDH on a MXene surface, followed by a low temperature *in situ* solid phase reaction. The final NFPS showed nano-mosaic shapes instead of the original TM-LDHS nanosheets, which had a unique electronic structure and extremely high electrochemically active surface area, leading to excellent overall water splitting activity in 1 M KOH.

$MoS_2$ shows favorable activity for the HER in acidic electrolytes due to the near-optimal hydrogen adsorption free energy. However, the HER kinetics of $MoS_2$ under alkaline conditions are sluggish due to the inferior ability for water dissociation.[133] FeOOH shows much stronger adsorption of hydroxyl species, enabling it to be effective for water dissociation. Unfortunately, the OER activity of FeOOH is much inferior due to its strong interaction with hydroxyl species. Xu *et al.*[134] found that coupling FeOOH with $MoS_2$ could not only promote the alkaline HER activity of $MoS_2$ by accelerating water dissociation, but also enhance the OER activity of FeOOH through the electronic modulation by $MoS_2$ (Fig. 17a). This one-stone-two-birds effect enabled the hybrid $MoS_2$/FeOOH to show outstanding HER and OER performance. The $MoS_2$/FeOOH was further coupled with 3D $Ni_3S_2$ nanowires to fabricate the $Ni_3S_2$@$MoS_2$/FeOOH. The morphological characterization indicated that FeOOH nanosheets were intimately coupled with $MoS_2$ nanosheets (Fig. 17b). XPS analyses revealed electron transfer from Fe atoms to Mo atoms (Fig. 17c and d). The Mo sites with a lower state in $MoS_2$ had higher HER activity, and the Fe sites with a higher state in FeOOH had higher OER activity. Such electronic modulation of Fe and Mo centers in $Ni_3S_2$@$MoS_2$/FeOOH hybrids was beneficial to improving their HER and OER activities. $Ni_3S_2$@$MoS_2$/FeOOH as an OER catalyst showed the lowest Tafel slope of 49 mV $dec^{-1}$, lower than that of $Ni_3S_2$/FeOOH (56 mV $dec^{-1}$) and $Ni_3S_2$@$MoS_2$ (114.0 mV $dec^{-1}$). Meanwhile, the catalyst exhibited a very low overpotential of 282 mV at a high current density of 100 mA $cm^{-2}$. Impressively, as an HER catalyst, $Ni_3S_2$@$MoS_2$/FeOOH could output a current density of 100 mA $cm^{-2}$ at a low overpotential of 177 mV, showing excellent electrocatalytic HER performance. Furthermore, as a bifunctional electrocatalyst, the electrocatalyst required only a small battery voltage of 1.57 V at 10 mA $cm^{-2}$. Han *et al.*[135] developed a composite catalyst consisting of perovskite oxide ($La_{0.5}Sr_{0.5}CoO_{3-\delta}$, LSC) and potassium ionically bonded molybdenum diselenide (K–$MoSe_2$) as a bifunctional catalyst for integral hydrolyzation (Fig. 17e). It is found that the LSC/K–$MoSe_2$ system had the characteristics of multi-direction charge transfer phenomena, including bidirectional charge transfer from K to $MoSe_2$ and from LSC to $MoSe_2$ (Fig. 17f), which endowed $MoSe_2$ with an electron-rich surface and increased electrical conductivity to improve the HER kinetics (Fig. 17g and h). Besides, the improvement of the electrophilicity of LSC improved the adsorption capacity of oxygen producing intermediates on the catalyst surface, thus improving the performance of the OER (Fig. 17i). Furthermore, LSC/K–$MoSe_2$ exhibited remarkable chronopotentiometry stability over 2500 h at a high current density of 100 mA $cm^{-2}$.

### 4.3 Interface formation

Interface engineering can create new active sites and promote electron transfer, thus boosting the efficiency of water

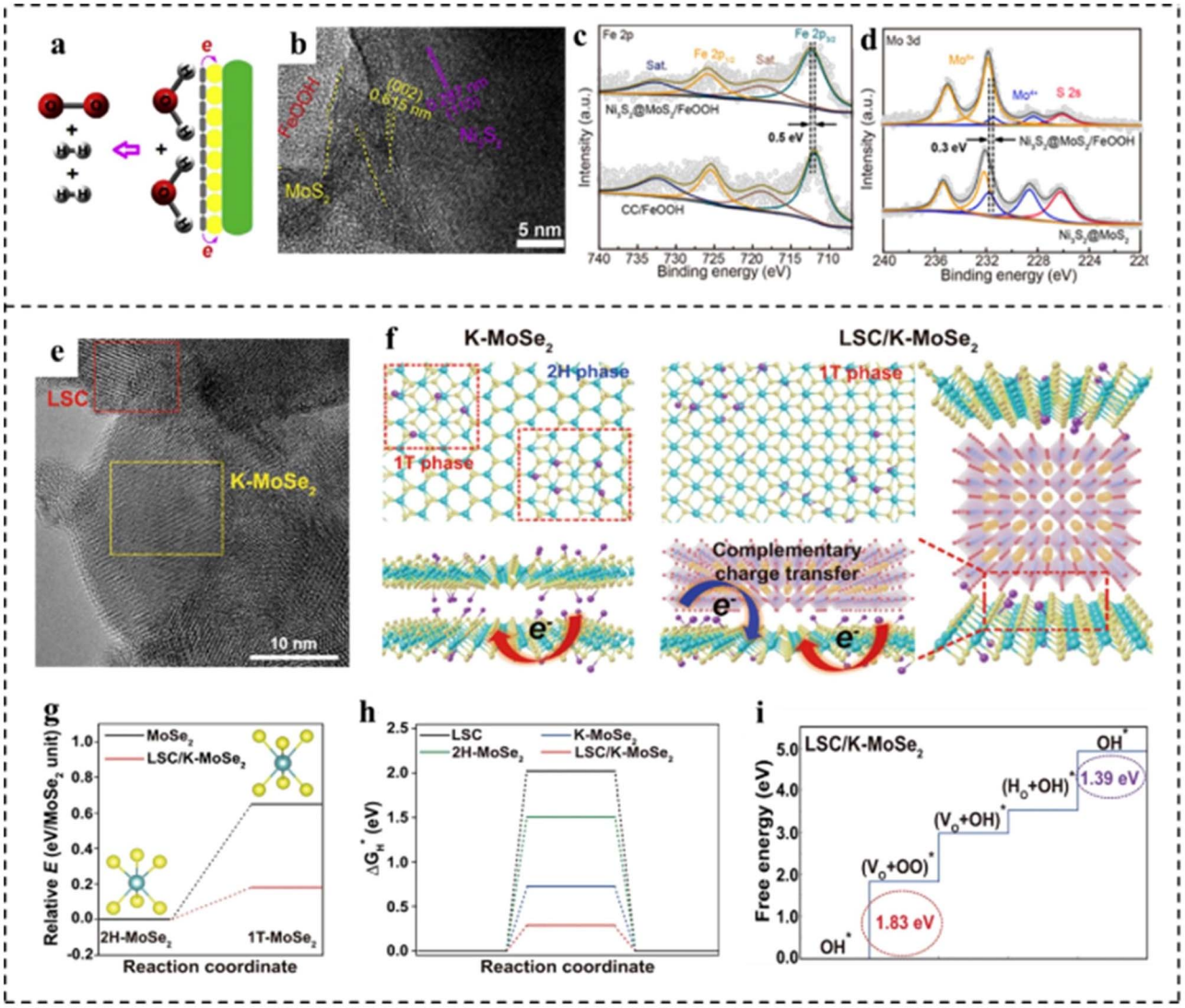


Fig. 17 (a) Schematic diagram for the overall water splitting mechanism of $Ni_3S_2$@$MoS_2$/FeOOH. (b) HRTEM image of $Ni_3S_2$@$MoS_2$/FeOOH. (c) Fe 2p XPS spectra of $Ni_3S_2$@$MoS_2$/FeOOH and FeOOH on carbon cloth (FeOOH/CC). (d) Mo 3d XPS spectra of $Ni_3S_2$@$MoS_2$/FeOOH and $Ni_3S_2$@$MoS_2$. Reproduced with permission from ref. 134. Copyright 2019, Elsevier. (e) HRTEM image of LSC/K–$MoSe_2$. (f) Schematic of the atomic structure and charge transfer effect for K–$MoSe_2$ and LSC/K–$MoSe_2$. Complementary charge transfer in LSC/K–$MoSe_2$ can modulate the electronic structure of $MoSe_2$, increasing the 1T-$MoSe_2$ ratio in the heterostructure. (g) Relative energies of 1T-$MoSe_2$ in the monolayer structure (black line) and LSC/K–$MoSe_2$ heterostructure (red line) compared to the energy of the 2H–$MoSe_2$ monolayer. (h) Free energy diagrams for the HER for LSC, 2H–$MoSe_2$, K–$MoSe_2$, and LSC/K–$MoSe_2$. (i) Free energy diagrams for the OER for LSC/K–$MoSe_2$. Reproduced with permission from ref. 135. Copyright 2021, Springer Nature.

splitting.[136,137] Moreover, the generated synergetic effects between different interfaces tailor the electronic structures of catalysts and the modulated electronic structure in turn influences the overall performance in electrocatalysis. Owing to the ultrathin properties of 2D components, most atoms in 2D layers can participate in the interface structure, which may lead to more pronounced interface effects on the modulation of electronic structures than in the ontology.[138,139] For example, Wu constructed a rich crystalline-amorphous boundary into ultrathin Ni-ZIF/Ni–B nanosheets.[140] DFT calculations indicated that the crystalline-amorphous interface not only reduced the energy barrier for the formation of *OH, but also reduced the reaction free energy from *O to *OOH. Besides, an optimal $\Delta G_{H^*}$ that was closer to zero implied its higher catalytic HER activity (Fig. 18a and b). Benefiting from the interface engineering, the Ni-ZIF/Ni–B nanosheets required an $\eta_{10}$ of 67 mV for the HER and an $\eta_{10}$ of 234 mV for the OER. Furthermore Ni-ZIF/Ni–B@NF as a bifunctional electrocatalyst for overall water splitting achieved an $\eta_{10}$ of 1.54 V. Sapra *et al.*[141] used interfacial engineering of the basal planes of $MoSe_2$ nanosheets (NSs) with $Cu_2S$ nanocrystals (NCs) to obviously promote the water splitting rate under alkaline conditions (Fig. 18c and d). In their work, the interface between the $MoSe_2$ NSs and $Cu_2S$ NCs increased the number of OER active sites, as shown in Fig. 18e

 

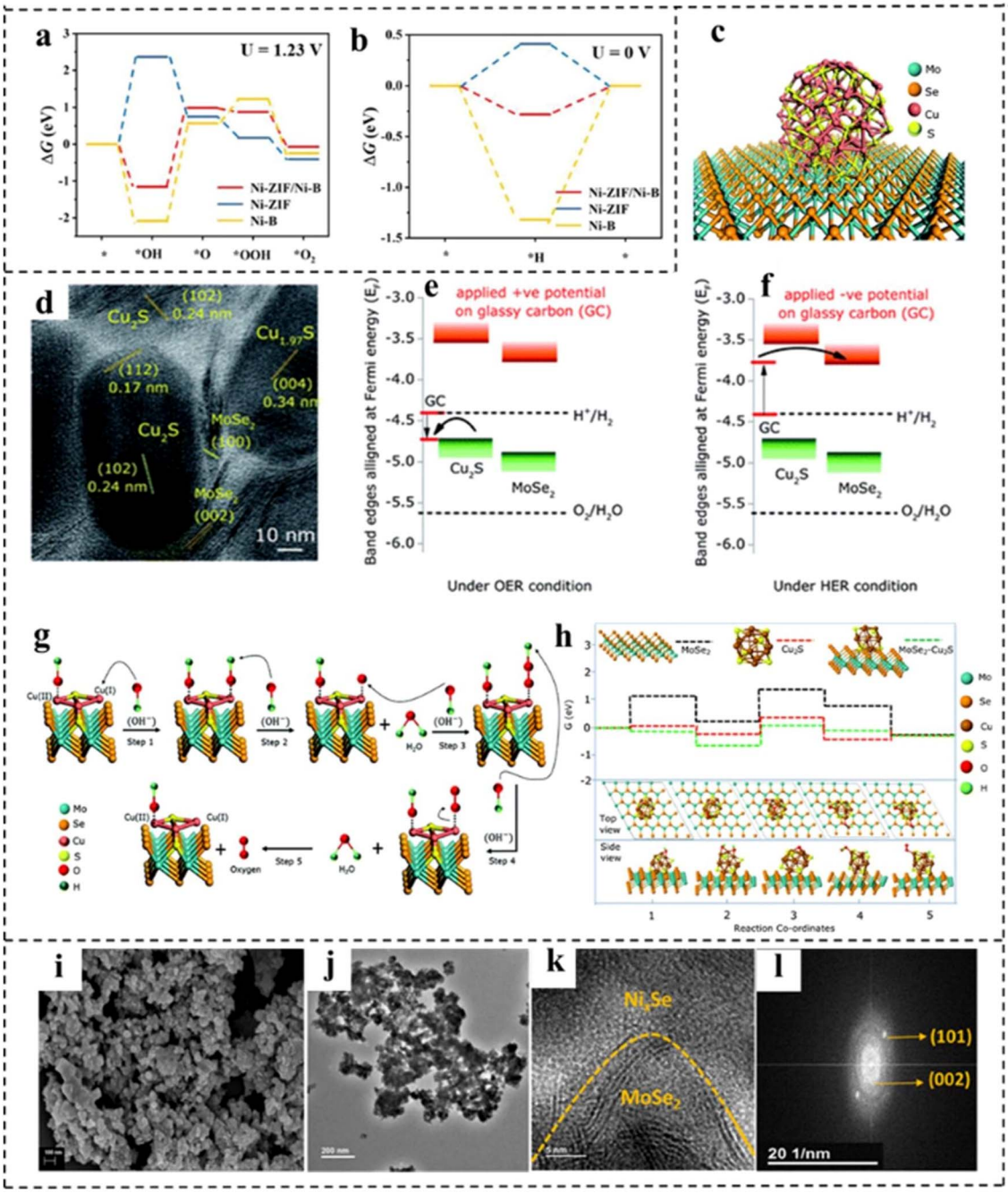


Fig. 18 (a) The calculated free–energy diagram of the OER and (b) the HER of Ni-ZIF/Ni–B and other control materials. Reproduced with permission from ref. 140. Copyright 2020, Wiley-VCH. (c) Schematic illustration of $MoSe_2$–$Cu_2S$ NHSs. (d) HRTEM image of $MoSe_2$–$Cu_2S$ NHSs. Schematic illustration of the energy band alignment of $MoSe_2$–$Cu_2S$ NHSs in (e) the OER *via* $Cu_2S$ and (f) the HER *via* $MoSe_2$. (g) Schematic illustration of the mechanism of the OER. (h) Free energy profiles of the reactants, intermediates and products of the OER for $MoSe_2$ NSs, $Cu_2S$ NCs and $MoSe_2$–$Cu_2S$ NHSs. Reproduced with permission from ref. 141. Copyright 2021, Royal Society of Chemistry. (i–k) SEM, TEM, and HRTEM images, and (l) fast Fourier transformation of the $Ni_{0.85}Se$–$MoSe_2$ interfacial structure. Reproduced with permission from ref. 142. Copyright 2021, American Chemical Society.

and f. The type-II alignment of nanoheterostructures (NHSs) formed an in-built potential at the interfaces, which helped to facilitate interfacial charge transfer at the junctions of two constituents. DFT calculations revealed (Fig. 18g and h) that due to the presence of type II NHSs, $Cu_2S$ NCs formed a built-in electric field at the junction, making them more electrophilic. This made the catalytic active site of NHSs more favorable for surface adsorption and conversion. The internal electric field at the interface significantly reduced the energy barrier for the formation of OH*, O*, OOH* and other intermediates, thus promoting the OER. Due to the increased number of active sites and the modulation of the electronic structure, $MoSe_2$–$Cu_2S$

NHSs exhibited higher OER activity with an $\eta_{10}$ of 264 mV. Also, the built-in electric field also greatly promoted the HER activity of $MoSe_2$–$Cu_2S$ NHSs owing to the reduction of the kinetic energy barrier. Mahalingam and coworkers[142] introduced $Ni_{0.75}Se$ nanoparticles into $MoSe_2$ to construct a $Ni_{0.85}Se/MoSe_2$ interface, which served as an active site for water splitting. The synthesized interfacial structure was composed of interlinked $Ni_{0.85}Se$ nanoparticles and $MoSe_2$ thin slices with abundant heterojunctions. As shown in Fig. 18i–l, SEM and TEM revealed distinguishable interfaces (boundaries) between $Ni_{0.85}Se$ particles and $MoSe_2$ flakes. Electrochemical investigations showed that the alkaline HER activity of the $Ni_{0.85}Se/MoSe_2$ interface structure was significantly increased, which was attributed to the efficient hydrolysis dissociation process on the $Ni_{0.85}Se$ promoter in the interface structure and the exposure of more $MoSe_2$ catalytically active sites (edges). In addition, the prepared $Ni_{0.85}Se/MoSe_2$ showed high OER activity. An alkaline electrolysis cell was constructed with $Ni_{0.85}Se/MoSe_2$ and $Ni_{0.75}Se$ as the cathode and anode, showing a voltage of 1.7 V at 10 mA $cm^{-2}$.

Interfacial engineering can be used to enhance the performance of overall water splitting. However, the heterogeneous interface and its microenvironment are complex, which makes the study of the catalytic reaction mechanism difficult. Besides, because of the simplification and idealization of the constructed model in theoretical calculations, there is still a gap between the heterogeneous interface model and the actual catalyst's interface. This makes it difficult for theoretical calculations to accurately reveal the real catalytic mechanism.

### 4.4 Defect engineering

Introducing defects into catalysts is another important strategy to enhance intrinsic activity. With the introduction of defect structures, the electronic configurations of catalyst sites are effectively tuned to facilitate the formation and transformation of intermediate states, thereby promoting specific electrochemical reactions. In most cases, defects are generally regarded as active sites for electrocatalytic processes due to the regulation of localized electronic and surface configurations.[143,144] According to their sizes, defects in catalytic materials can be mainly divided into four types, including 0 D point defects, 1D line defects, 2D plane defects and 3D volume defects. Point defects can be further divided into three types: vacancy defects, impurity doped defects and metal defect coordination structures.[145] First, defect engineering can provide more active sites for electrocatalysts, thus directly refining their

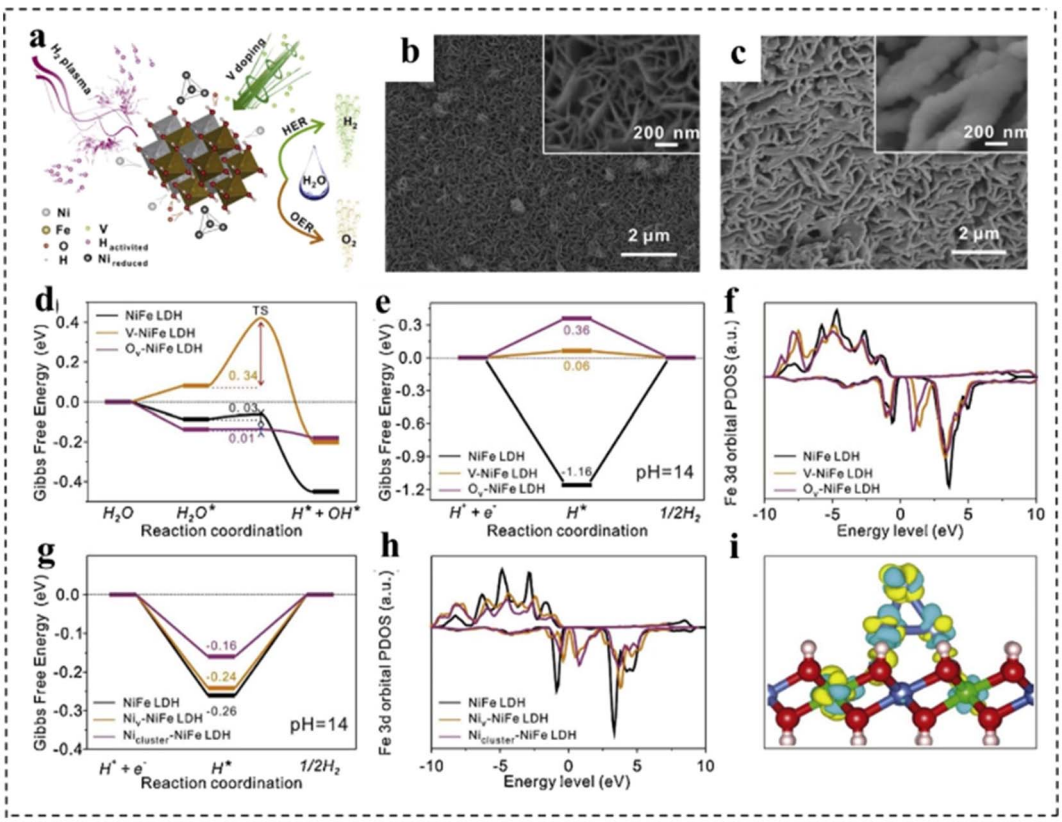


Fig. 19 (a) Schematic illustration of the reaction mechanism of the P–V–NiFe LDH NSA. SEM images of (b) the NiFe LDH NSA and (c) the P–V–NiFe LDH NSA. The diagram of calculated adsorption free energy on the NiFe LDH (100) plane (d and e) and (001) plane (g) for the Volmer step (d) and Tafel step (e and g). The calculated projected densities of states of the Fe 3d orbital on the NiFe LDH (100) plane (f) and (001) plane (h). (i) The differential charge density contour plot after supporting Ni clusters on the NiFe LDH (001) plane. The cyan and yellow colors indicate the decrease and increase in the electron density, respectively. The 3D isosurface value is set as 0.007 e $Å^{-3}$. Blue balls: Ni atoms; green balls: Fe atoms; red balls: O atoms; pink balls: H atoms. Reproduced with permission from ref. 147. Copyright 2020, Elsevier.

 

electrocatalytic activity. Second, the rational construction of composites can form a large number of defective structures, which can effectively adjust the electronic structure and promote electron transfer, thus improving the efficiency of overall water separation. Third, catalytically active substances can be anchored on defective carriers, which can directly maximize the exposure of active substances and improve the charge transfer between catalytically active substances.

At present, various strategies for defect construction have been used in 2D bifunctional electrocatalysts, such as high temperature reduction and plasma treatment.[146] For example, Yu *et al.*[147] synthesized a P–V–NiFe LDH nanosheet array (NSA) with multiple vacancies through a cation doping combined with plasma reduction strategy. As a bifunctional electrocatalyst, the P–V–NiFe LDH NSA shows a small $\eta_{10}$ of 200 mV with significant stability for 1000 h. The authors discussed in detail the role of vacancy defects through structural analysis and theoretical simulation. As shown in Fig. 19a–c, the surface of NiFe LDH became rough after introducing defects. Meanwhile, DFT calculations revealed that V doping, oxygen vacancies (Ov) and Ni vacancies (Niv) could optimize the hydrogen adsorption (Fig. 19e and g) and increase the conductivity (Fig. 19f, h and i). In addition, Ov and Niv were favorable for $H_2O$ adsorption and dissociation in the HER, and the V-doping and Ov efficiently reduced the energy barrier for the formation of O* in the OER (Fig. 19d).

Besides, the rational construction of composites can lead to the formation of defective structures. For example, Qi *et al.*[148] prepared defect-rich $MoS_2/NiS_2$ nanosheets by annealing Ni–Mo precursors with sublimated sulfur in an Ar atmosphere (Fig. 20a). Fig. 20b–e demonstrate that $MoS_2/NiS_2$ had numerous defects and interfaces, providing more catalytic sites for electrocatalytic reactions. The mismatch between $MoS_2$ and $NiS_2$ created a distinct heterointerface that could induce abundant defects and disordered structures. Raman spectroscopy (Fig. 20f) further indicated the existence of abundant low-coordination Mo–S edge sites in $MoS_2/NiS_2$, while XPS demonstrated the existence of sulfur defects (Fig. 20g). This structure facilitated the generation of electrons and accelerated the electrocatalytic process, thereby improving the activities of the

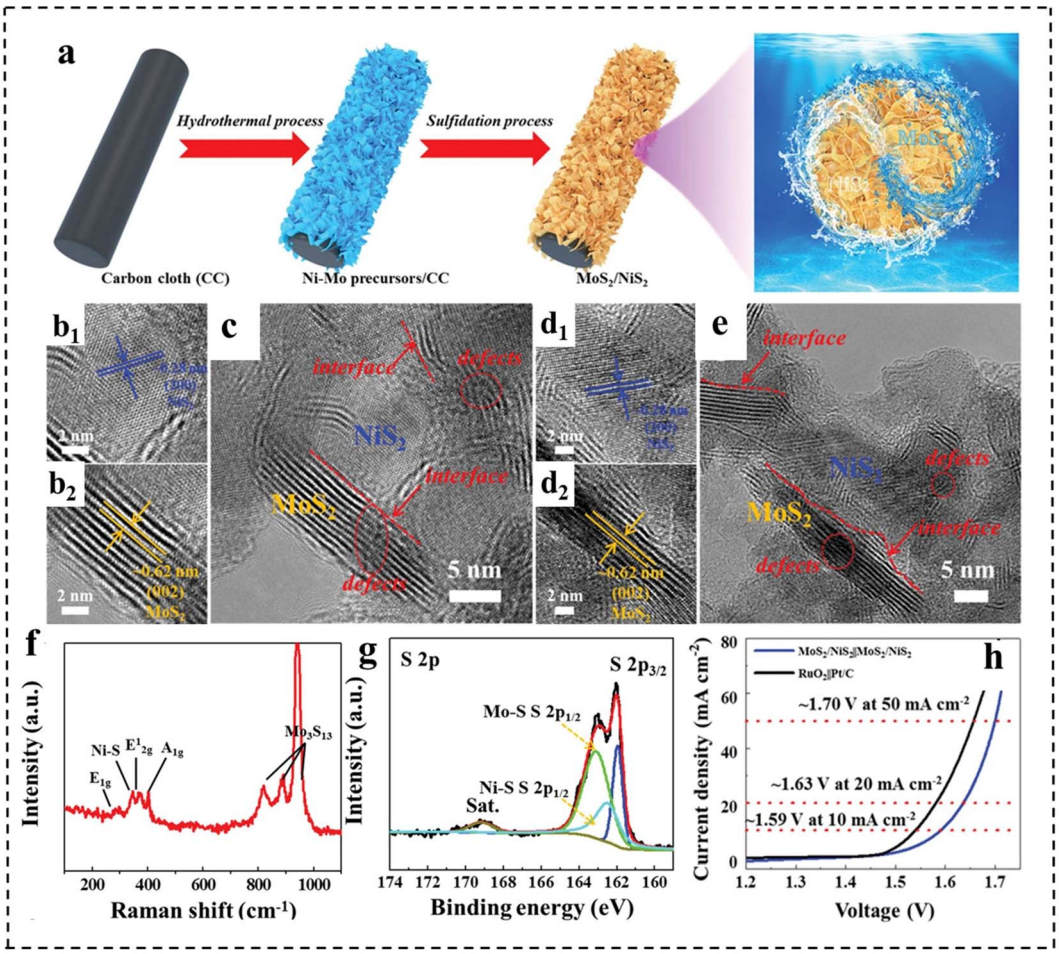


Fig. 20 (a) Schematic illustration for the formation of defect-rich heterogeneous $MoS_2/NiS_2$ nanosheets. (b–e) HRTEM images of $MoS_2/NiS_2$ nanosheets. (f) Raman spectrum of $MoS_2/NiS_2$ nanosheets. (g) High-resolution XPS profiles of S 2p in $MoS_2/NiS_2$ nanosheets. (h) Polarization curves of optimal $MoS_2/NiS_2$ nanosheets and $RuO_2$||Pt/C for overall water splitting. Reproduced with permission from ref. 148. Copyright 2019, Wiley-VCH.

HER and OER. As a result, the optimized $MoS_2/NiS_2$ nanosheets showed a low voltage of 1.59 V at 10 mA $cm^{-2}$ (Fig. 20h).

Despite great advances, the reported strategies used to prepare defective catalysts, such as chemical etching and plasma etching, still present significant challenges in controlling site-specific defect construction and precisely controlling defect concentration.[149] In addition, the most frequently reported defect-based materials rarely meet the practical needs of industrial production. Therefore, further research and development of methods for large-scale preparation of defect catalysts are necessary. Meanwhile, some defects are unstable, making the catalyst prone to failure during the catalytic process. Therefore, the stabilization of defects is also a concern of defect engineering. Whether stable defect structures can be maintained or reconstituted during the actual catalytic process needs to be further investigated. Besides, the quantification and precise control of defects are a challenge.

### 4.5 Morphology modulation

Morphological engineering of 2D nanomaterials as bifunctional electrocatalysts for full water splitting plays an important role in achieving excellent electrocatalytic performance, because it is closely related to the physical specific surface area, the number of exposed active centers for catalytic reactions, and the mass transfer during electrochemical reactions. Generally, morphological engineering is not as effective as other means of increasing the intrinsic activity of the catalyst. In this section, we present the rational design and effects of morphological engineering with typical examples.[150,151] For example, Li *et al.*[152] reported a simple and controllable strategy to prepare $CoSe_2$ with different shapes. By adjusting the additional amount of $NH_4F$, $CoSe_2$ samples (spherical, linear and rod-like) were successfully synthesized (Fig. 21a–c). Among them, the $CoSe_2$ microspheres were revealed to have a regular sea urchin shape and hollow structure, resulting in a large specific surface area and a large number of channels to promote mass transfer efficiency. Therefore, the $CoSe_2$ sphere electrocatalyst showed excellent catalytic performance for the OER and HER under alkaline and acidic conditions, respectively (*e.g.*, an $\eta_{10}$ of 325 mV and a Tafel slope of 80 mV $dec^{-1}$ for the OER in alkaline media and an $\eta_{10}$ of 167 mV and a Tafel slope of 38 mV $dec^{-1}$ for the HER in acidic media, respectively).

Morphological regulation strategies can also be used to ameliorate the catalytic performance of MOFs. The small pore size is one of the major challenges in using MOFs for electrocatalysis, which inhibits the effective mass transport of electrolytes to active centers and diffusion of products, resulting in hindered electrocatalyst performance. This is especially

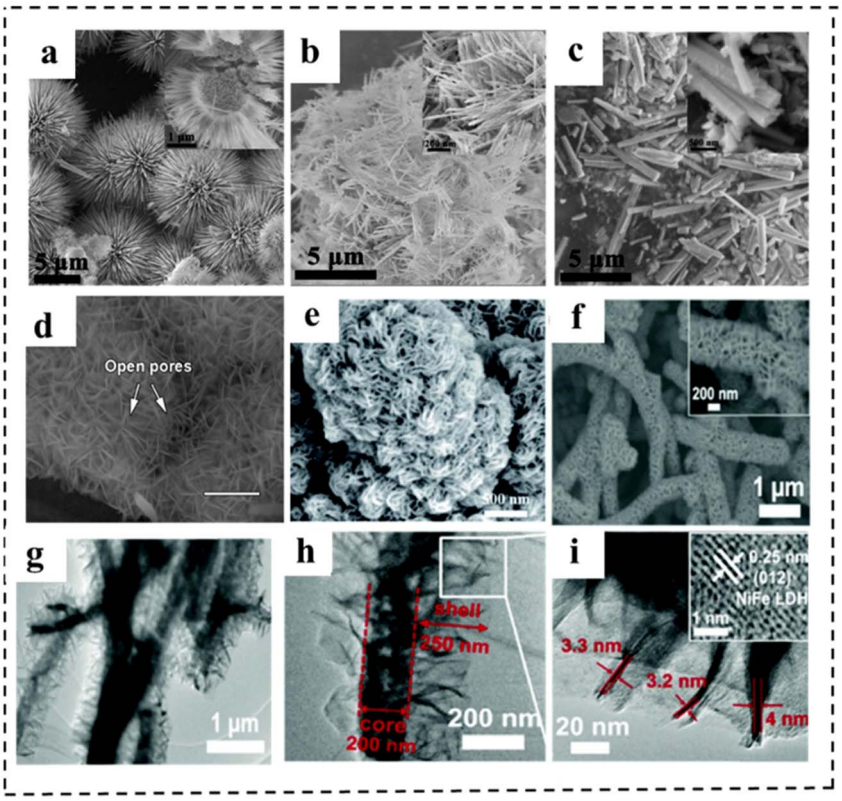


Fig. 21 (a–c) SEM images of $CoSe_2$ spheres, wires and rods. Reproduced with permission from ref. 152. Copyright 2019, Elsevier. (d) SEM image (scale bars are 300 mm) of NiFe-MOF/NF. Reproduced with permission from ref. 153. Copyright 2017, Springer Nature. (e) SEM images of NiFe (dobpdc). Reproduced with permission from ref. 154. Copyright 2020, Royal Society of Chemistry. (f) SEM images of Cu@NiFe LDH at high magnification. (g–i) TEM images of Cu@NiFe LDH. (j) Detailed image of the squared part in the image of Cu@NiFe LDH to show the lattice fringe (inset). Reproduced with permission from ref. 155. Copyright 2017, Royal Society of Chemistry.

 

a problem in water electrolysis because the electrode products are $O_2$ and $H_2$ gases, which have the potential to cover the active sites of MOFs and inhibit ions' transport. To solve this issue, increasing the pore size of the MOF is a good solution. Zhao *et al.*[153] prepared a MOF with different hierarchical-scale porosities (several-hundred-micrometre macropores, tens-of-nanometre open pores, several-nanometre mesopores and intrinsic microporosity). The extra-large macropores of nickel foam could facilitate the mass transport of electrolytes and gaseous products, while the open pores between vertically aligned nanosheets, and small mesopores and micropores of the MOF provided enormous, highly accessible active sites and short ion diffusion pathways (Fig. 21d). Thus, the resulting NiFe-MOF catalyst exhibited excellent activities and stabilities for the OER ($\eta_{10}$: 240 mV) and HER ($\eta_{10}$: 134 mV). The electrolytic cell was demonstrated to show excellent catalytic activity, delivering a voltage of 1.55 V at 10 mA $cm^{-2}$ in 0.1 M KOH. Similarly, Lin *et al.*[154] synthesized NiFe (dobpdc) by utilizing a longer organic linker ($H_4$dobpdc). The NiFe (dobpdc) had a yarn-ball like structure assembled from 2D nanosheet subunits, and it possessed a high surface area and large pore size (Fig. 21e). This allowed adequate contact with $H_2O$ and enlarged the electrochemically active surface area, resulting in an accelerated water splitting reaction. This bifunctional NiFe (dobpdc) MOF electrocatalyst exhibited low overpotentials for the OER and HER, respectively. Moreover, DFT calculations revealed that the longer ligand ($dobpdc_4$) had the ability of extracting and releasing charges during the steps of (* → OH*) and (OH* → O*), respectively.

Besides, 3D core–shell nanoarchitectures grown on conductive substrates are of great interest due to their large surface areas, efficient electron transfer, and intimate access to the electrolyte. For example, Yu *et al.*[155] fabricated a 3D catalyst with a core–shell nanostructure, in which few-layer NiFe LDH nanosheets uniformly and vertically grew on Cu nanowire (NW) cores supported on Cu foam (Fig. 21f). The TEM image in Fig. 21g–i showed that the nanosheets were interconnected with each other, forming a highly porous surface morphology, which offered many channels for electrolyte diffusion and gaseous product release. Also, such a 3D nanostructure facilitated efficient electron transfer from the inner metallic Cu NWs to the outer shell of the NiFe LDH layer. Thus, the Cu@NiFe LDH exhibited outstanding OER as well as HER performance in alkaline medium. Using them as bifunctional catalysts for overall water splitting, a voltage of 1.54 V at 10 mA $cm^{-2}$ was achieved with excellent durability, which was much better than the benchmark of $IrO_2(+)||Pt(-)$ electrodes.

## 5. Conclusion and outlook

Electrolysis of water is an important technology for green hydrogen production facing energy and environmental crisis. In the past decades, great efforts and breakthroughs have been made in the design and optimization of bifunctional electrocatalysts. This paper systematically reviews the classification, controlled synthesis and formation mechanisms of 2D nanomaterials including graphitized carbon nitride, layered double hydroxide, transition metal dichalcogenide, transition metal carbon/nitride and 2D metal–organic framework compounds. The strategies for tuning the catalytic activity of 2D bifunctional electrocatalysts (doping, defect engineering, nanocomposite construction, interface formation, and morphology engineering), and the effects on the electrocatalytic performance of the OER and HER are then discussed: doping and defect engineering are implemented to fine-tune the electronic configuration and states; nanocomposites and interfaces are constructed to synergistically boost water splitting performance; morphology engineering is utilized to expose more active sites. In practical applications, the combination of different strategies is more effective in balancing OER and HER performances. Despite the promising progress in the development of 2D electrocatalysts for full water splitting, there are still some problems to be solved in the practical application of water electrolysis.

First of all, the current yields, quality and quantity of 2D nanomaterials are still insufficient to meet industrial and commercial demands, so developing effective tactics for the large-scale production of high-quality 2D materials is needed. Therefore, there is a great need to optimize the current synthesis methods. Besides, the long-term stability and toxicity of the synthetic routes are also of great concern. The ideal 2D catalysts should be easy to prepare on a large scale, highly stable, environmentally friendly and cost-effective. Thinner even monolayered or more defective 2D bifunctional electrocatalysts can achieve high electrocatalytic performance, but such electrocatalysts often show problems such as inactivation caused by structural instability, especially under harsh reaction conditions. In this regard, it is crucial to seek new methods to synthesize inherently stable 2D electrocatalysts or develop efficient protection strategies to stabilize 2D electrocatalysts during electrocatalytic processes. Especially, balancing and optimizing the activity and stability in industrial-scale applications, like in strong alkali electrolytes, under high temperature or high current density (*e.g.*, 1 A $cm^{-2}$) conditions, are also a challenge. Second, the current characterization of 2D bifunctional electrocatalysts is usually based on non-in-situ methods. However, the chemical reaction process is dynamic, and the intermediates as one of the most important factors cannot be detected using these methods, leading to a poor understanding of their working mechanism. Therefore, *in situ* characterization and tracer techniques such as *in situ* Raman, *in situ* Fourier transform infrared and *in situ* XAFS should be developed to obtain real-time observations and investigations on the intermediates, the valence and electron distribution of the catalytically active sites, and the catalytic pathway, thus constructing the relationships between the structure and performance of 2D bifunctional electrocatalysts. This will help to get an in-depth understanding on the fundamental principles of 2D bifunctional electrocatalysts during full water splitting at the atomic level. Third, the gap between the molecular configurations in theoretical calculations and the actual products in experiments hinders the investigation of the activity origin in many electrocatalytic processes. This is due in part to the limitations of current computing power and the complexity of currently

available candidates with multiple physico-chemical properties. As a result, the fundamental basis for the active origin is still highly needed. Finally, 2D bifunctional electrocatalysts show good catalytic activity in alkaline water electrolysis, but in practical applications, electrocatalysts that are universal to pH are still a challenge. 2D bifunctional electrocatalysts for pH generalization or seawater electrolysis are still quite limited in practical applications.

With the development of materials science and chemistry, we believe that any kind of 2D nanomaterial can be prepared into a single layer or a few atomic layers using appropriate methods. Going forward, the combination of theoretical calculations, experimental measurements, and advanced spectroscopic characterization may be the best way to design and develop novel 2D bifunctional electrocatalysts. Bridging the gap between theory and experiment for 2D electrocatalysts is critical and will require close collaboration between materials scientists, computational chemists and electrochemists. We believe that the systematic and comprehensive content of this review will stimulate wider research and attention to the further advances of 2D nanomaterials as bifunctional electrocatalysts for full water splitting.

## Conflicts of interest

The authors declare no conflict of interest.

## Acknowledgements

We are grateful for financial support from the National Natural Science Foundation of China (52002015, 22275010, and 22105016), and the Research Fund Program of Guangdong Provincial Key Laboratory of Fuel Cell Technology (FC202203).

## References

1 M.-Q. Zhao, Q. Zhang, J.-Q. Huang and F. Wei, *Adv. Funct. Mater.*, 2012, **22**, 675–694.
2 X. Zou and Y. Zhang, *Chem. Soc. Rev.*, 2015, **44**, 5148–5180.
3 S. J. Davis, N. S. Lewis, M. Shaner, S. Aggarwal, D. Arent, I. L. Azevedo, S. M. Benson, T. Bradley, J. Brouwer, Y.-M. Chiang, C. T. M. Clack, A. Cohen, S. Doig, J. Edmonds, P. Fennell, C. B. Field, B. Hannegan, B.-M. Hodge, M. I. Hoffert, E. Ingersoll, P. Jaramillo, K. S. Lackner, K. J. Mach, M. Mastrandrea, J. Ogden, P. F. Peterson, D. L. Sanchez, D. Sperling, J. Stagner, J. E. Trancik, C.-J. Yang and K. Caldeira, *Science*, 2018, **360**, eaas9793.
4 Y. Li, R. Zhang, J. Li, J. Liu, Y. Miao, J. Guo and M. Shao, *Chin. Chem. Lett.*, 2021, **32**, 1165–1168.
5 S. Chu and A. Majumdar, *Nature*, 2012, **488**, 294–303.
6 L. Meng and L. Li, *Nano Res. Energy*, 2022, **1**, e9120020.
7 M. Wang, L. Chen and L. Sun, *Energy Environ. Sci.*, 2012, **5**, 6763–6778.
8 C. Wang, Q. Zhang, B. Yan, B. You, J. Zheng, L. Feng, C. Zhang, S. Jiang, W. Chen and S. He, *Nano-Micro Lett.*, 2023, **15**, 52.
9 B. You and Y. Sun, *Acc. Chem. Res.*, 2018, **51**, 1571–1580.
10 E. Fabbri, A. Habereder, K. Waltar, R. Kötz and T. J. Schmidt, *Catal. Sci. Technol.*, 2014, **4**, 3800–3821.
11 Y. Jiao, Y. Zheng, M. Jaroniec and S. Z. Qiao, *Chem. Soc. Rev.*, 2015, **44**, 2060–2086.
12 H. Xu, H. Shang, C. Wang and Y. Du, *Coord. Chem. Rev.*, 2020, **418**, 213374.
13 C. Wang, A. Schechter and L. Feng, *Nano Res. Energy*, 2023, e9120056.
14 J. Safaei and G. Wang, *Nano Res. Energy*, 2022, **1**, e9120008.
15 X. Zhou, T. Yang, T. Li, Y. Zi, S. Zhang, L. Yang, Y. Liu, J. Yang and J. Tang, *Nano Res. Energy*, 2023, **2**, e9120086.
16 M. Kopp, D. Coleman, C. Stiller, K. Scheffer, J. Aichinger and B. Scheppat, *Int. J. Hydrogen Energy*, 2017, **42**, 13311–13320.
17 H. Yang, Z. Chen, P. Guo, B. Fei and R. Wu, *Appl. Catal., B*, 2020, **261**, 118240.
18 C. Liao, B. Yang, N. Zhang, M. Liu, G. Chen, X. Jiang, G. Chen, J. Yang, X. Liu, T.-S. Chan, Y.-J. Lu, R. Ma and W. Zhou, *Adv. Funct. Mater.*, 2019, **29**, 1904020.
19 D. Xing, Y. Wang, P. Zhou, Y. Liu, Z. Wang, P. Wang, Z. Zheng, H. Cheng, Y. Dai and B. Huang, *Appl. Catal., B*, 2020, **278**, 119295.
20 J. Wu, M. Liu, K. Chatterjee, K. P. Hackenberg, J. Shen, X. Zou, Y. Yan, J. Gu, Y. Yang, J. Lou and P. M. Ajayan, *Adv. Mater. Interfaces*, 2016, **3**, 1500669.
21 C. Chen, X. Xie, B. Anasori, A. Sarycheva, T. Makaryan, M. Zhao, P. Urbankowski, L. Miao, J. Jiang and Y. Gogotsi, *Angew. Chem., Int. Ed.*, 2018, **57**, 1846–1850.
22 X. Li, Q. Hu, H. Yang, T. Ma, X. Chai and C. He, *Chin. Chem. Lett.*, 2022, **33**, 3657–3671.
23 K. S. Novoselov, A. K. Geim, S. V. Morozov, D. Jiang, Y. Zhang, S. V. Dubonos, I. V. Grigorieva and A. A. Firsov, *Science*, 2004, **306**, 666–669.
24 A. Bruix, J. T. Margraf, M. Andersen and K. Reuter, *Nat. Catal.*, 2019, **2**, 659–670.
25 J. H. Montoya, L. C. Seitz, P. Chakthranont, A. Vojvodic, T. F. Jaramillo and J. K. Nørskov, *Nat. Mater.*, 2017, **16**, 70–81.
26 C. Zhang, Z. Guo, Y. Tan, C. Yu, K. Liu, C. Yu and L. Jiang, *Nano Res. Energy*, 2023, **2**, e9120063.
27 Y. Chen, Z. Fan, Z. Zhang, W. Niu, C. Li, N. Yang, B. Chen and H. Zhang, *Chem. Rev.*, 2018, **118**, 6409–6455.
28 R. Sun, W. Guo, X. Han and X. Hong, *Chem. Res. Chin. Univ.*, 2020, **36**, 597–610.
29 Z. Li, L. Zhai, Y. Ge, Z. Huang, Z. Shi, J. Liu, W. Zhai, J. Liang and H. Zhang, *Natl. Sci. Rev.*, 2022, **9**, nwab142.
30 G. Zhao, J. Zou, X. Chen, J. Yu and F. Jiao, *Chem. Eng. J.*, 2020, **397**, 125407.
31 A. I. Khan, A. Ragavan, B. Fong, C. Markland, M. O'Brien, T. G. Dunbar, G. R. Williams and D. O'Hare, *Ind. Eng. Chem. Res.*, 2009, **48**, 10196–10205.
32 S. Jiang, Y. Liu, W. Xie and M. Shao, *J. Energy Chem.*, 2019, **33**, 125–129.
33 Z. Shan, P. S. Archana, G. Shen, A. Gupta, M. G. Bakker and S. Pan, *J. Am. Chem. Soc.*, 2015, **137**, 11996–12005.

 

34 J.-H. Choy, S.-Y. Kwak, Y.-J. Jeong and J.-S. Park, *Angew. Chem., Int. Ed.*, 2000, **39**, 4041–4045.
35 L. Zhang, J. Liang, L. Yue, K. Dong, J. Li, D. Zhao, Z. Li, S. Sun, Y. Luo, Q. Liu, G. Cui, A. Ali Alshehri, X. Guo and X. Sun, *Nano Res. Energy*, 2022, **1**, e9120028.
36 Z. Lu, L. Qian, Y. Tian, Y. Li, X. Sun and X. Duan, *Chem. Commun.*, 2016, **52**, 908–911.
37 T. Wang, G. Nam, Y. Jin, X. Wang, P. Ren, M. G. Kim, J. Liang, X. Wen, H. Jang, J. Han, Y. Huang, Q. Li and J. Cho, *Adv. Mater.*, 2018, **30**, e1800757.
38 C. X. Zhao, J. N. Liu, J. Wang, D. Ren, J. Yu, X. Chen, B. Q. Li and Q. Zhang, *Adv. Mater.*, 2021, **33**, e2008606.
39 L. Zhou, C. Zhang, Y. Zhang, Z. Li and M. Shao, *Adv. Funct. Mater.*, 2021, **31**, 2009743.
40 B. Liu, T. Xiao, X. Sun, H.-Q. Peng, X. Wang, Y. Zhao, W. Zhang and Y.-F. Song, *J. Mater. Chem. A*, 2022, **10**, 19649–19661.
41 S. Jiang, T. Xiao, C. Xu, S. Wang, H. Q. Peng, W. Zhang, B. Liu and Y. F. Song, *Small*, 2023, **19**, 2208027.
42 M. Groenewolt and M. Antonietti, *Adv. Mater.*, 2005, **17**, 1789–1792.
43 D. M. Teter and R. J. Hemley, *Science*, 1996, **271**, 53–55.
44 Y. Zhao, J. Zhang and L. Qu, *ChemNanoMat*, 2015, **1**, 298–318.
45 A. Zambon, J. M. Mouesca, C. Gheorghiu, P. A. Bayle, J. Pécaut, M. Claeys-Bruno, S. Gambarelli and L. Dubois, *Chem. Sci.*, 2016, **7**, 945–950.
46 C. Tan, X. Cao, X. J. Wu, Q. He, J. Yang, X. Zhang, J. Chen, W. Zhao, S. Han, G. H. Nam, M. Sindoro and H. Zhang, *Chem. Rev.*, 2017, **117**, 6225–6331.
47 E. Kroke, M. Schwarz, E. Horath-Bordon, P. Kroll, B. Noll and A. D. Norman, *New J. Chem.*, 2002, **26**, 508–512.
48 X. Wang, K. Maeda, A. Thomas, K. Takanabe, G. Xin, J. M. Carlsson, K. Domen and M. Antonietti, *Nat. Mater.*, 2009, **8**, 76–80.
49 S. M. Lyth, Y. Nabae, S. Moriya, S. Kuroki, M. a. Kakimoto, J.-i. Ozaki and S. J. J. o. P. C. C. Miyata, *J. Phys. Chem.*, 2009, **113**, 20148–20151.
50 Z. Su, Q. Huang, Q. Guo, S. J. Hoseini, F. Zheng and W. Chen, *Nano Res. Energy*, 2023, **2**, e9120078.
51 O. M. Yaghi, G. Li and H. Li, *Nature*, 1995, **378**, 703–706.
52 X. Kong, G. Liu, H.-Q. Peng, Z. Xu, S. Bu, B. Liu and W. Zhang, *J. Mater. Chem. A*, 2022, **10**, 6596–6606.
53 L. Sun, M. G. Campbell and M. Dincă, *Angew. Chem., Int. Ed.*, 2016, **55**, 3566–3579.
54 Y. Zhi, Z. Wang, H.-L. Zhang and Q. Zhang, *Small*, 2020, **16**, 2001070.
55 M. Zhao, Y. Huang, Y. Peng, Z. Huang, Q. Ma and H. Zhang, *Chem. Soc. Rev.*, 2018, **47**, 6267–6295.
56 S. Zhao, Y. Wang, J. Dong, C.-T. He, H. Yin, P. An, K. Zhao, X. Zhang, C. Gao, L. Zhang, J. Lv, J. Wang, J. Zhang, A. M. Khattak, N. A. Khan, Z. Wei, J. Zhang, S. Liu, H. Zhao and Z. Tang, *Nat. Energy*, 2016, **1**, 16184.
57 Q. Shao, J. Yang and X. Huang, *Chem. - Eur. J.*, 2018, **24**, 15143–15155.
58 T. Ahmad, S. Liu, M. Sajid, K. Li, M. Ali, L. Liu and W. Chen, *Nano Res. Energy*, 2022, **1**, e9120021.
59 X. F. Lu, B. Y. Xia, S.-Q. Zang and X. W. Lou, *Angew. Chem., Int. Ed.*, 2020, **59**, 4634–4650.
60 M. Chhowalla, H. S. Shin, G. Eda, L.-J. Li, K. P. Loh and H. Zhang, *Nat. Chem.*, 2013, **5**, 263–275.
61 Q. H. Wang, K. Kalantar-Zadeh, A. Kis, J. N. Coleman and M. S. Strano, *Nat. Nanotechnol.*, 2012, **7**, 699–712.
62 M. Pumera, Z. Sofer and A. Ambrosi, *J. Mater. Chem. A*, 2014, **2**, 8981–8987.
63 J. Tabernor, P. Christian and P. O'Brien, *J. Mater. Chem. A*, 2006, **16**, 2082–2087.
64 W. Qiu, M. Xu, X. Yang, F. Chen, Y. Nan, J. Zhang, H. Iwai and H. Chen, *J. Mater. Chem.*, 2011, **21**, 13327–13333.
65 M. Naguib, M. Kurtoglu, V. Presser, J. Lu, J. Niu, M. Heon, L. Hultman, Y. Gogotsi and M. W. Barsoum, *Adv. Mater.*, 2011, **23**, 4248–4253.
66 B. Anasori, Y. Xie, M. Beidaghi, J. Lu, B. C. Hosler, L. Hultman, P. R. C. Kent, Y. Gogotsi and M. W. Barsoum, *ACS Nano*, 2015, **9**, 9507–9516.
67 J. Halim, S. Kota, M. R. Lukatskaya, M. Naguib, M.-Q. Zhao, E. J. Moon, J. Pitock, J. Nanda, S. J. May, Y. Gogotsi and M. W. Barsoum, *Adv. Funct. Mater.*, 2016, **26**, 3118–3127.
68 S. Lai, J. Jeon, S. K. Jang, J. Xu, Y. J. Choi, J.-H. Park, E. Hwang and S. Lee, *Nanoscale*, 2015, **7**, 19390–19396.
69 Q. Hu, D. Sun, Q. Wu, H. Wang, L. Wang, B. Liu, A. Zhou and J. He, *J. Phys. Chem. A*, 2013, **117**, 14253–14260.
70 M. Khazaei, A. Mishra, N. S. Venkataramanan, A. K. Singh and S. Yunoki, *Curr. Opin. Solid State Mater. Sci.*, 2019, **23**, 164–178.
71 A. D. Dillon, M. J. Ghidiu, A. L. Krick, J. Griggs, S. J. May, Y. Gogotsi, M. W. Barsoum and A. T. Fafarman, *Adv. Funct. Mater.*, 2016, **26**, 4162–4168.
72 Z. W. Seh, K. D. Fredrickson, B. Anasori, J. Kibsgaard, A. L. Strickler, M. R. Lukatskaya, Y. Gogotsi, T. F. Jaramillo and A. Vojvodic, *ACS Energy Lett.*, 2016, **1**, 589–594.
73 T. Y. Ma, J. L. Cao, M. Jaroniec and S. Z. Qiao, *Angew. Chem., Int. Ed.*, 2016, **55**, 1138–1142.
74 L. Li, R. Ma, Y. Ebina, N. Iyi and T. Sasaki, *Chem. Mater.*, 2005, **17**, 4386–4391.
75 F. Song and X. Hu, *Nat. Commun.*, 2014, **5**, 4477.
76 A. Ambrosi, Z. Sofer and M. Pumera, *Small*, 2015, **11**, 605–612.
77 X. Zhang, X. Xie, H. Wang, J. Zhang, B. Pan and Y. Xie, *J. Am. Chem. Soc.*, 2013, **135**, 18–21.
78 S. Yang, Y. Gong, J. Zhang, L. Zhan, L. Ma, Z. Fang, R. Vajtai, X. Wang and P. M. Ajayan, *Adv. Mater.*, 2013, **25**, 2452–2456.
79 Q. Lin, L. Li, S. Liang, M. Liu, J. Bi and L. Wu, *Appl. Catal., B*, 2015, **163**, 135–142.
80 Y. Wang, Y. Zhang, Z. Liu, C. Xie, S. Feng, D. Liu, M. Shao and S. Wang, *Angew. Chem., Int. Ed.*, 2017, **56**, 5867–5871.
81 R. B. Nielsen, K. O. Kongshaug and H. Fjellvåg, *J. Mater. Chem.*, 2008, **18**, 1002–1007.
82 P. Amo-Ochoa, L. Welte, R. Gonzalez-Prieto, P. J. Sanz Miguel, C. J. Gomez-Garcia, E. Mateo-Marti, S. Delgado, J. Gomez-Herrero and F. Zamora, *Chem. Commun.*, 2010, **46**, 3262–3264.

83 Y. Peng, Y. Li, Y. Ban, H. Jin, W. Jiao, X. Liu and W. Yang, *Science*, 2014, **346**, 1356–1359.
84 S. Zhao, Y. Wang, J. Dong, C.-T. He, H. Yin, P. An, K. Zhao, X. Zhang, C. Gao, L. Zhang, J. Lv, J. Wang, J. Zhang, A. M. Khattak, N. A. Khan, Z. Wei, J. Zhang, S. Liu, H. Zhao and Z. Tang, *Nat. Energy*, 2016, **1**, 16184.
85 Y. Liu, H. Cheng, M. Lyu, S. Fan, Q. Liu, W. Zhang, Y. Zhi, C. Wang, C. Xiao, S. Wei, B. Ye and Y. Xie, *J. Am. Chem. Soc.*, 2014, **136**, 15670–15675.
86 T. P. Nguyen, S. Choi, J.-M. Jeon, K. C. Kwon, H. W. Jang and S. Y. Kim, *J. Phys. Chem. C*, 2016, **120**, 3929–3935.
87 P. J. S. Jin-Chong Tan, E. G. Bithell and A. K. Cheetham, *ACS Nano*, 2012, **6**, 615–621.
88 Y. Peng, Y. Li, Y. Ban and W. Yang, *Angew. Chem., Int. Ed.*, 2017, **56**, 9757–9761.
89 J. Xu, L. Zhang, R. Shi and Y. Zhu, *J. Mater. Chem. A*, 2013, **1**, 14766–14772.
90 W.-J. Song, *Talanta*, 2017, **170**, 74–80.
91 J. Huang, Y. Li, R.-K. Huang, C.-T. He, L. Gong, Q. Hu, L. Wang, Y.-T. Xu, X.-Y. Tian, S.-Y. Liu, Z.-M. Ye, F. Wang, D.-D. Zhou, W.-X. Zhang and J.-P. Zhang, *Angew. Chem., Int. Ed.*, 2018, **57**, 4632–4636.
92 Y. A. Eshete, N. Ling, S. Kim, D. Kim, G. Hwang, S. Cho and H. Yang, *Adv. Funct. Mater.*, 2019, **29**, 1904504.
93 M. A. Lukowski, A. S. Daniel, F. Meng, A. Forticaux, L. Li and S. Jin, *J. Am. Chem. Soc.*, 2013, **135**, 10274–10277.
94 A. Y. S. Eng, A. Ambrosi, Z. Sofer, P. Šimek and M. Pumera, *ACS Nano*, 2014, **8**, 12185–12198.
95 D. Voiry, M. Salehi, R. Silva, T. Fujita, M. Chen, T. Asefa, V. B. Shenoy, G. Eda and M. Chhowalla, *Nano Lett.*, 2013, **13**, 6222–6227.
96 X. Wang, C. Chi, K. Zhang, Y. Qian, K. M. Gupta, Z. Kang, J. Jiang and D. Zhao, *Nat. Commun.*, 2017, **8**, 14460.
97 H. Y. Changgu Lee, L. E. Brus, T. F. Heinz, J. Hone and S. Ryu, *ACS Nano*, 2010, **4**, 2695–2700.
98 M. Naguib, M. Kurtoglu, V. Presser, J. Lu, J. Niu, M. Heon, L. Hultman, Y. Gogotsi and M. W. Barsoum, *Adv. Mater.*, 2011, **23**, 4248–4253.
99 O. M. Michael Naguib, J. Carle, V. Presser, J. Lu, L. Hultman, Y. Gogotsi and M. W. Barsoum, *ACS Nano*, 2012, **6**, 1322–1331.
100 M. Naguib, J. Come, B. Dyatkin, V. Presser, P.-L. Taberna, P. Simon, M. W. Barsoum and Y. Gogotsi, *Electrochem. Commun.*, 2012, **16**, 61–64.
101 S. Yang, P. Zhang, F. Wang, A. G. Ricciardulli, M. R. Lohe, P. W. M. Blom and X. Feng, *Angew. Chem., Int. Ed.*, 2018, **57**, 15491–15495.
102 S. Liu, J. Zhu, M. Sun, Z. Ma, K. Hu, T. Nakajima, X. Liu, P. Schmuki and L. Wang, *J. Mater. Chem. A*, 2020, **8**, 2490–2497.
103 A. Carne, C. Carbonell, I. Imaz and D. Maspoch, *Chem. Soc. Rev.*, 2011, **40**, 291–305.
104 M. M. Rao, B. R. Reddy, M. Jayalakshmi, V. S. Jaya and B. Sridhar, *Mater. Res. Bull.*, 2005, **40**, 347–359.
105 X. Wang, J. Zhang, S. Yang, H. Yan, X. Hong, W. Dong, Y. Liu, B. Zhang and Z. Wen, *Electrochim. Acta*, 2019, **295**, 1–6.
106 Z. Hu, E. M. Mahdi, Y. Peng, Y. Qian, B. Zhang, N. Yan, D. Yuan, J.-C. Tan and D. Zhao, *J. Mater. Chem. A*, 2017, **5**, 8954–8963.
107 F.-L. Li, P. Wang, X. Huang, D. J. Young, H.-F. Wang, P. Braunstein and J.-P. Lang, *Angew. Chem., Int. Ed.*, 2019, **58**, 7051–7056.
108 A. Y. S. Eng, J. L. Cheong and S. S. Lee, *Appl. Mater. Today*, 2019, **16**, 529–537.
109 M. Zhao, Y. Wang, Q. Ma, Y. Huang, X. Zhang, J. Ping, Z. Zhang, Q. Lu, Y. Yu, H. Xu, Y. Zhao and H. Zhang, *Adv. Mater.*, 2015, **27**, 7372–7378.
110 C. Cong, J. Shang, X. Wu, B. Cao, N. Peimyoo, C. Qiu, L. Sun and T. Yu, *Adv. Opt. Mater.*, 2014, **2**, 131–136.
111 Y. Zhang, Y. Zhang, Q. Ji, J. Ju, H. Yuan, J. Shi, T. Gao, D. Ma, M. Liu, Y. Chen, X. Song, H. Y. Hwang, Y. Cui and Z. Liu, *ACS Nano*, 2013, **7**, 8963–8971.
112 J. Chen, X. Zhao, S. J. R. Tan, H. Xu, B. Wu, B. Liu, D. Fu, W. Fu, D. Geng, Y. Liu, W. Liu, W. Tang, L. Li, W. Zhou, T. C. Sum and K. P. Loh, *J. Am. Chem. Soc.*, 2017, **139**, 1073–1076.
113 H. Kumar, B. Bharti, S. Aslam, R. U. R. Sagar, K. Wang, L. Gan, P. Hua, X. Zeng and Y. Su, *Int. J. Energy Res.*, 2020, **44**, 7846–7854.
114 F. Chen, X. Jiang, J. Shao, B. Lu, L. Fu, S. Zhao and W. Su, *CrystEngComm*, 2021, **23**, 1345–1351.
115 Z. Zhang, P. Chen, X. Duan, K. Zang, J. Luo and X. Duan, *Science*, 2017, **357**, 788–792.
116 H. Li, T. Thanh-Nhan, B.-J. Lee, C. Zhang, J.-D. Park, T.-H. Kang and J.-S. Yu, *ACS Appl. Mater. Interfaces*, 2017, **9**, 20294–20298.
117 C. Tang, H. S. Wang, H. F. Wang, Q. Zhang, G. L. Tian, J. Q. Nie and F. Wei, *Adv. Mater.*, 2015, **27**, 4516–4522.
118 D. Wang, Q. Li, C. Han, Q. Lu, Z. Xing and X. Yang, *Nat. Commun.*, 2019, **10**, 3899.
119 H. Zong, K. Yu and Z. Zhu, *Electrochim. Acta*, 2020, **353**, 136598.
120 G. Qian, J. Chen, T. Yu, J. Liu, L. Luo and S. Yin, *Nano-Micro Lett.*, 2021, **14**, 20.
121 H. Y. Wang, L. Wang, J. T. Ren, W. W. Tian, M. L. Sun and Z. Y. Yuan, *Nano-Micro Lett.*, 2023, **15**, 155.
122 X.-P. Li, L.-R. Zheng, S.-J. Liu, T. Ouyang, S. Ye and Z.-Q. Liu, *Chin. Chem. Lett.*, 2022, **33**, 4761–4765.
123 Y. Wen, Z. Wei, J. Liu, R. Li, P. Wang, B. Zhou, X. Zhang, J. Li and Z. Li, *J. Energy Chem.*, 2021, **52**, 412–420.
124 B. Liu, Y. F. Zhao, H. Q. Peng, Z. Y. Zhang, C. K. Sit, M. F. Yuen, T. R. Zhang, C. S. Lee and W. J. Zhang, *Adv. Mater.*, 2017, **29**, 1606521.
125 Y. Jia, L. Zhang, G. Gao, H. Chen, B. Wang, J. Zhou, M. T. Soo, M. Hong, X. Yan, G. Qian, J. Zou, A. Du and X. Yao, *Adv. Mater.*, 2017, **29**, 1700017.
126 X. Zhang, J. Fan, X. Lu, Z. Han, C. Cazorla, L. Hu, T. Wu and D. Chu, *Chem. Eng. J.*, 2021, **415**, 129048.
127 R. Yang, Y. Zhou, Y. Xing, D. Li, D. Jiang, M. Chen, W. Shi and S. Yuan, *Appl. Catal., B*, 2019, **253**, 131–139.
128 B. Jiang, T. Wang, Y. Cheng, F. Liao, K. Wu and M. Shao, *ACS Appl. Mater. Interfaces*, 2018, **10**, 39161–39167.

 

129 J. Rashid, N. Parveen, T. u. Haq, A. Iqbal, S. H. Talib, S. U. Awan, N. Hussain and M. Zaheer, *ChemCatChem*, 2018, **10**, 5587–5592.
130 M. Yu, J. Zheng and M. Guo, *J. Energy Chem.*, 2022, **70**, 472–479.
131 L. Yan, B. Zhang, S. Wu and J. Yu, *J. Mater. Chem. A*, 2020, **8**, 14234–14242.
132 C.-F. Du, K. N. Dinh, Q. Liang, Y. Zheng, Y. Luo, J. Zhang and Q. Yan, *Adv. Energy Mater.*, 2018, **8**, 1801127.
133 J. Staszak-Jirkovský, C. D. Malliakas, P. P. Lopes, N. Danilovic, S. S. Kota, K.-C. Chang, B. Genorio, D. Strmcnik, V. R. Stamenkovic, M. G. Kanatzidis and N. M. Markovic, *Nat. Mater.*, 2016, **15**, 197–203.
134 M. Zheng, K. Guo, W.-J. Jiang, T. Tang, X. Wang, P. Zhou, J. Du, Y. Zhao, C. Xu and J.-S. Hu, *Appl. Catal., B*, 2019, **244**, 1004–1012.
135 N. K. Oh, J. Seo, S. Lee, H.-J. Kim, U. Kim, J. Lee, Y.-K. Han and H. Park, *Nat. Commun.*, 2021, **12**, 4606.
136 Y. Jiang, Y. Li, Y. Jiang, X. Liu, W. Shen, M. Li and R. He, *Chin. Chem. Lett.*, 2022, **33**, 4003–4007.
137 P. Wang, Y. Luo, G. Zhang, Z. Chen, H. Ranganathan, S. Sun and Z. Shi, *Nano-Micro Lett.*, 2022, **14**, 120.
138 L. Yan, L. Cao, P. Dai, X. Gu, D. Liu, L. Li, Y. Wang and X. Zhao, *Adv. Funct. Mater.*, 2017, **27**, 1703455.
139 X. Gao, H. Zhang, Q. Li, X. Yu, Z. Hong, X. Zhang, C. Liang and Z. Lin, *Angew. Chem., Int. Ed.*, 2016, **55**, 6290–6294.
140 H. Xu, B. Fei, G. Cai, Y. Ha, J. Liu, H. Jia, J. Zhang, M. Liu and R. Wu, *Adv. Energy Mater.*, 2020, **10**, 1902714.
141 M. S. Hassan, P. Basera, S. Gahlawat, P. P. Ingole, S. Bhattacharya and S. Sapra, *J. Mater. Chem. A*, 2021, **9**, 9837–9848.
142 H. R. Inta, S. Ghosh, A. Mondal, G. Tudu, H. V. S. R. M. Koppisetti and V. Mahalingam, *ACS Appl. Energy Mater.*, 2021, **4**, 2828–2837.
143 Z. Xiao, C. Xie, Y. Wang, R. Chen and S. Wang, *J. Energy Chem.*, 2021, **53**, 208–225.
144 Q. Xie, Z. Cai, P. Li, D. Zhou, Y. Bi, X. Xiong, E. Hu, Y. Li, Y. Kuang and X. Sun, *Nano Res.*, 2018, **11**, 4524–4534.
145 C. Xie, D. Yan, H. Li, S. Du, W. Chen, Y. Wang, Y. Zou, R. Chen and S. Wang, *ACS Catal.*, 2020, **10**, 11082–11098.
146 X. Kong, Q. Gao, S. Bu, Z. Xu, D. Shen, B. Liu, C.-S. Lee and W. Zhang, *Mater. Today Energy*, 2021, **21**, 100784.
147 Y. Tang, Q. Liu, L. Dong, H. B. Wu and X.-Y. Yu, *Appl. Catal., B*, 2020, **266**, 118627.
148 J. Lin, P. Wang, H. Wang, C. Li, X. Si, J. Qi, J. Cao, Z. Zhong, W. Fei and J. Feng, *Adv. Sci.*, 2019, **6**, 1900246.
149 Y. J. Wu, J. Yang, T. X. Tu, W. Q. Li, P. F. Zhang, Y. Zhou, J. F. Li, J. T. Li and S. G. Sun, *Angew. Chem., Int. Ed.*, 2021, **60**, 26829–26836.
150 Y. Guo, Z. Yao, C. Shang and E. Wang, *ACS Appl. Mater. Interfaces*, 2017, **9**, 39312–39317.
151 X. Zhao, P. Gao, Y. Yan, X. Li, Y. Xing, H. Li, Z. Peng, J. Yang and J. Zeng, *J. Mater. Chem. A*, 2017, **5**, 20202–20207.
152 K. Lan, J. Li, Y. Zhu, L. Gong, F. Li, P. Jiang, F. Niu and R. Li, *J. Colloid Interface Sci.*, 2019, **539**, 646–653.
153 J. Duan, S. Chen and C. Zhao, *Nat. Commun.*, 2017, **8**, 15341.
154 L. Qi, Y.-Q. Su, Z. Xu, G. Zhang, K. Liu, M. Liu, E. J. M. Hensen and R. Y.-Y. Lin, *J. Mater. Chem. A*, 2020, **8**, 22974–22982.
155 L. Yu, H. Zhou, J. Sun, F. Qin, F. Yu, J. Bao, Y. Yu, S. Chen and Z. Ren, *Energy Environ. Sci.*, 2017, **10**, 1820–1827.